Article:
Zhang, B., Yao, S., Poulton, S.W. et al. (2023) Widespread marine euxinia along the western Yangtze Platform caused by oxygen minimum zone expansion during the Capitanian mass extinction. Global and Planetary Change, 230. 104273. ISSN: 0921-8181

https://doi.org/10.1016/j.gloplacha.2023.104273

Widespread marine euxinia along the western Yangtze Platform caused by oxygen minimum zone expansion during the Capitanian mass extinction

Bolin Zhang[1, 2, 3*], Suping Yao[3], Simon W. Poulton[4], Paul B. Wignall[4], Tianchen He[5], Yijun Xiong[4], Wenxuan Hu[3]

[1] State Key Laboratory of Oil and Gas Reservoir Geology and Exploitation & Institute of Sedimentary Geology, Chengdu University of Technology, Chengdu 610059, China

[2] Key Laboratory of Deep-time Geography and Environment Reconstruction and Applications of Ministry of Natural Resources, Chengdu University of Technology, Chengdu 610059, China

[3] Key Laboratory of Surficial Geochemistry, Ministry of Education, School of Earth Sciences and Engineering, Nanjing University, Nanjing 210023, China

[4] School of Earth and Environment, University of Leeds, Leeds LS2 9JT, UK

[5] College of Oceanography, Hohai University, Nanjing 210024, China

corresponding author: zhangbolin@cdut.edu.cn (B. Zhang)

Abstract

The development of widespread marine anoxic and/or euxinic conditions has been proposed as a likely driver of the mid-Capitanian mass extinction. However, the driving mechanisms and spatiotemporal evolution of anoxia/euxinia remain poorly constrained. In order to decipher changes in marine redox conditions and their possible influence on the mid-Capitanian biotic crisis, we applied multiple geochemical indicators to three sections across a shelf-to-basin transect in the Middle Permian Kuhfeng and Lower Yinping formations of the Lower Yangtze Basin, South China. Our integrated Fe speciation and redox-sensitive trace element data suggest that euxinic waters dynamically coexisted at intermediate depths on the western margin of the Yangtze Platform, with oxygenated surface waters and ferruginous deeper waters providing compelling evidence for a redox structure similar to an oxygen minimum zone (OMZ). The synthesis of a five-stage spatiotemporal evolution of redox conditions, coupled with changes in upwelling and hydrographic restriction, indicates particularly intensified euxinia and an expanded OMZ across the shelf-basin transect during the middle Capitanian. Long-lasting anoxia-euxinia was likely maintained by enhanced phosphorus cycling, with sluggish ocean circulation due to collapsed upwelling and enhanced restriction under climate warming intensifying the euxinic conditions. Through a comparison of available global data, we infer that widespread anoxia-euxinia was prevalent in the middle Capitanian due to expanded OMZ conditions. Expanded anoxia and euxinia in shelf and slope environments occurred concurrently with an ongoing biotic crisis suggesting that these redox changes were a contributory factor.

Keywords: Middle Permian; South China; Redox conditions; Fe speciation

1. Introduction

The mid-Capitanian (or end-Guadalupian) biotic crisis, is one of the most severe biotic events of the Phanerozoic (comparable to the "Big Five" Phanerozoic mass extinctions; e.g., Stanley, 2016), although its timing, nature and causes are all debated. Proposed causal mechanisms include regression (e.g., Jin et al., 1994; Chen et al., 2009), global cooling (e.g., Isozaki et al. 2007), marine anoxia (e.g., Zhang et al., 2015; Wei et al., 2016, 2019; Smith et al., 2020), or the effects of the Emeishan Large Igneous Province eruptions (ELIP, e.g., Kaiho et al., 2005, 2023; Sun et al., 2010; Wignall et al., 2009; Huang et al., 2019). However, while no consensus has been reached, the development of marine anoxia has frequently been invoked as consequential (e.g., Saitoh et al., 2014; Bond et al., 2015; Wei et al., 2016, 2019; Fujisaki et al., 2019; Smith et al., 2020; Song et al., 2023).

During the Capitanian, marine anoxia was apparently widespread, but with distinct temporal and regional variability (e.g., Zhang et al., 2019a; Fujisaki et al., 2019; Song et al., 2023). Previous studies have shown that anoxic-euxinic conditions were present prior to the late Capitanian at intermediate ocean depths around the margin of the South China continent (Saitoh et al. 2014; Wei et al., 2019; Zhang et al., 2019a, b, 2021). Expansion of this mid-depth water oxygen minimum zone (OMZ) saw the spread of oxygen-poor conditions into shallow waters prior to and/or during the extinction (Saitoh et al. 2014; Bond et al. 2015; Zhang et al. 2015; Wei et al., 2016, 2019). However, better constraints on the spatial distribution of anoxia-euxinia in the water column and its dynamic evolution through this period are required to understand its potential role as a kill mechanism during the mid-Capitanian crisis.

The driving mechanisms responsible for the development of intensified anoxic and/or euxinic conditions during the mid-Capitanian extinction are not fully understood. Divergent opinions propose either the expansion of OMZ-type conditions caused by increased upwelling and productivity (e.g., Saitoh et al., 2014; Zhang et al., 2019a), or decreased upwelling but increased terrigenous nutrient input during global warming (e.g., Chen et al., 2011; Zhang et al., 2021). Alternatively, basinal anoxia may have expanded during marine regression (e.g., Wei et al., 2019; Smith et al., 2020). Modern oceanic-climate models suggest that OMZ expansion can result in the shoaling of sulfidic waters (e.g., Stramma et al., 2008), while upwelling-driven OMZ expansion and oceanic anoxia have been linked to other mass extinctions (e.g., Late Ordovician-Early Silurian, Zou et al., 2018). However, much less is known about the redox state and spatiotemporal evolution of Middle Permian upwelling-driven OMZ settings and controlling mechanisms.

Here, we aim to decipher spatiotemporal changes of marine redox conditions in the eastern Paleo-Tethys Ocean (South China) during the Middle Permian, and to evaluate the role of such changes in the mid-Capitanian crisis. We apply a multi-proxy approach based on iron speciation and redox-sensitive trace elements (particularly Mo and U) to analyze redox changes in three sections that accumulated along a shelf-to-basin transect in the Lower Yangtze upwelling region. A Middle Permian OMZ-type redox structure and its dynamic evolution are reconstructed.

2. Geological setting

2.1 Paleogeography and studied sections

During the Middle Permian, the Lower Yangtze Basin was located on the northwestern margin of the Yangtze Platform (South China) and was open to the Paleo-Tethys Ocean that lay to the northwest (Fig. 1a, Wang and Jin, 2000). A widespread upwelling system has been proposed to have developed along this margin throughout the Middle Permian (Kametaka et al. 2005; Yao et al. 2015; Shi et al., 2016; Zhang et al., 2021, 2023). This is confirmed by the lithological character of the strata, which are typical of those found beneath upwelling zones (e.g., phosphate nodules and rhythmic chert-mudstone couplets), the paleontological assemblage (radiolarians and sponge spicules), geochemical evidence (i.e., Cd/Mo > 0.1 and Co×Mn < 0.4), and the paleoenvironmental conditions (i.e., high surface primary productivity and middle water-depth anoxic conditions) as indicated by the studies on the Kuhfeng Formation (Lv and Zhai, 1990; Winguth et al., 2002; Kametaka et al., 2005; Lv et al., 2010; Yao et al., 2015; Shi et al., 2016; Zhang et al., 2018, 2021, 2022a, 2023). In addition, the Permian paleogeographic and paleoclimatic modeling predicted that over 70% of the areas along the northwestern margin of the Yangtze Platform were favorable locations for upwelling (Golonka et al., 1994).

A northwest-southeast transect through the Lower Yangtze basin captures a full range of settings from continental shelf, through slope to deep basin (Fig. 1b). Two well-exposed sections (Pingdingshan and Qinglongshan) and a newly-drilled core (Gangdi) (Fig. 2) provide a shelf-to-basin transect (Figs. 1b-c). The Pingdingshan (PDS) section was mainly deposited in an open-marine, lower slope–basin setting (Fig. 2) (Kametaka et al., 2005, 2009), whereas the Qinglongshan (QLS) section records sedimentary succession in relatively shallower water outer shelf facies (Fig. 2), although it was below fair-weather wave base and far from shore, on a broad continental shelf (Figs. 1d-e; Zhang et al., 2020). The Gangdi (GD) core accumulated on an open outer shelf setting with a good connection to the Paleo-Tethys Ocean during the early-middle Guadalupian (Figs. 1d and 2), but the location is inferred to have become silled later, during the Capitanian, due to tectonic intrashelf subsidence (Fig. 1e; Zhang et al., 2022b). An explanation of the above sedimentary environments can be found in Fig. 2 and Supplementary Tables S1-S3 and Fig. S1. In addition, previous studies have also confirmed that, based on typical minerals (e.g., glauconite pellets and phosphate nodules) and radiolarian faunas (He et al., 1999; Kametaka et al., 2005, 2009), the water depth range in the Lower Yangtze region during the deposition of the Kuhfeng Formation was approximately 50-500 m, which is comparable to the water depth (~100–900 m) at which the OMZ develops in the modern ocean (e.g., Scholz, 2018).

2.2 Age constraints and stratigraphic correlation

The Lower Yangtze Basin provides a relatively continuous Middle Permian stratigraphic record, with both deep (Kuhfeng Formation) and shallow (Yinping Formation) marine units. The Kuhfeng Formation consists of cyclically interbedded chert and mudstone, which are attributed to orbital forcing (Yao et al., 2015), whereas the Yinping Formation records shallow, coastal clastic deposition composed mainly of black to pale-grey mudstone, shale and siltstone (Zhang et al., 2020, 2021). The Kuhfeng Formation is subdivided into three lithologically-distinct members: the Lower Phosphate Nodule-bearing Mudstone Member (LPMM), the Middle Chert-Mudstone Member (MCMM), and the Upper Mudstone Member (UMM). The Lower Yinping Formation is divided into two members: the Lower Shale Member (LSM) and the Middle Shale Member (MSM) (Fig. 2). Intrabasinal correlation has been achieved using a well-established lith-, bio- and chemostratigraphic framework (Fig. 2; Zhang et al., 2020).

Conodonts (e.g., *Jinogondolella nankingensis*) and ammonoids (e.g., *Nodogastrioceras discum*, *Erinoceras sp*) discovered in the basal beds of the Kuhfeng Formation suggest an early Middle Permian age (e.g., Kametaka et al., 2009; Wu et al., 2017). Three radiolarian assemblage zones established in the Kuhfeng Formation also indicate a Roadian-Capitanian age (Fig. 2; Kametaka et al., 2009; Zhang et al., 2020). Furthermore, high-precision zircon U-Pb ages of 272.95 ± 0.11 Ma (Wu et al., 2017) and 261.08 ± 0.14 Ma (Wu, 2020) from tuff beds at the base and top of the Kuhfeng Formation, respectively, also suggest that the Kuhfeng Formation is of Middle Permian age and accumulated over 11 Myrs (Fig. 2). Finally, a high-resolution $\delta^{13}C_{org}$ chemostratigraphic framework through these studied sections (Zhang et al., 2020) can be correlated globally (Fig. 2). The negative excursions in $\delta^{13}C_{org}$ from the LPMM to the middle MCMM suggest a Roadian interval (e.g., Shen et al., 2020), which was followed by a Wordian–early Capitanian positive excursion in the upper MCMM and lower UMM (Fig. 2; Zhang et al., 2020). A subsequent negative $\delta^{13}C_{org}$ excursion, best seen in the upper UMM to the LSM of the GD core data (Fig. 2). This may coincide with the major negative shift in $\delta^{13}C_{carb}$ values of many worldwide sections (e.g., Wignall et al., 2009; Bond et al., 2010; Zhang et al., 2020), indicating the middle Capitanian interval. This inference is supported by boundary tuff U-Pb ages of 261.08 ± 0.14 Ma (Fig. 2; Wu, 2020), which is consistent with our previous LA-ICP-MS dating results (261.6 ± 1.6 Ma) on the same sample (PDS-5; Zhang et al., 2019b). Following this negative excursion, a rapid positive $\delta^{13}C_{org}$ shift in the MSM suggests the late Capitanian interval (Fig. 2).

3. Samples and methods

A total of 230 samples were collected at approximately 0.7–1.0 m intervals from the freshest exposures of the PDS section, GD core and QLS section. All samples were crushed and ground into powders for subsequent geochemical analyses. Total Al concentrations were determined by an ARL9900 X-ray fluorescence spectrometry (XRF), with analytical uncertainty < 1%, and trace elements were determined after bulk rock total dissolution on a Finnigan Element 2 inductively coupled plasma mass spectrometer (ICP-MS) with analytical precision better than 5%. Both Al concentration and trace elements were analysed at the State Key Laboratory for Mineral Deposits Research, Nanjing University. Detailed analytical methods for trace and major element analyses are in Supplementary Materials and Zhang et al. (2018).

Highly reactive iron (Fe_{HR}) was determined following the sequential extraction procedure of Poulton and Canfield (2005). The scheme determines operationally-defined Fe pools, and targets Fe in pyrite (Fe_{py}), ferric (oxyhydr)oxides (Fe_{ox}), magnetite (Fe_{mag}) and carbonate phases (Fe_{carb}). Concentrations of Fe_{carb}, Fe_{ox} and Fe_{mag} in sequential extracts were determined via atomic absorption spectrometry (AAS) at University of Leeds, with a relative standard deviation (RSD) of < 5% for all phases. Fe_{py} was extracted using the chromium reduction method (Canfield et al., 1986) and calculated stoichiometrically based on the pyrite sulfur concentration (S_{py}) assuming a 1:2 Fe:S molar ratio in pyrite. For elemental analyses of total iron (Fe_T), we used a multi-acid digestion (HNO_3-HF-$HClO_4$) on ashed samples (8 h at 550 °C) before quantification via AAS, with a RSD of < 5% (Alcott et al., 2020).

4. Proxy interpretation

Fe speciation and redox-sensitive trace elements (RSTEs, e.g., Mo and U) are widely used to diagnose local water column redox conditions during sediment deposition (e.g., Tribovillard et al., 2006; Poulton and Canfield, 2011; Scott and Lyons, 2012; Poulton, 2021). The combined use of these redox proxies can provide a robust evaluation of a range of local water-column redox conditions (e.g., Poulton and Canfield, 2011; Poulton, 2021).

Generally, Fe_{HR}/Fe_{T} ratios exceeding 0.38 imply anoxic water column conditions, whereas ratios below 0.22 indicate oxic conditions in the water column (Poulton and Canfield, 2011; Poulton, 2021). For anoxic samples, Fe_{Py}/Fe_{HR} ratios can distinguish euxinic conditions (> 0.8) and possibly euxinic conditions (0.6–0.8) from anoxic, ferruginous conditions (< 0.6) (Poulton, 2021). In addition, Fe_{T}/Al ratios can potentially provide information for evaluating water column redox conditions, since the ratio is commonly considered to remain unaffected by diagenesis (e.g., Lyons and Severmann, 2006). Fe_{T}/Al ratios above the average oxic Phanerozoic shale value (0.55 ± 0.11) may indicate anoxic water column conditions during deposition, when applied alongside other independent water column redox proxies (Clarkson et al., 2014; Poulton, 2021). However, it is increasingly apparent that Fe_{T}/Al ratios may be much more variable than previously thought, with a variety of studies identifying particularly low background ratios in sediments delivered to the marine realm, which may subsequently mask enrichments indicative of water column anoxia (e.g., Poulton et al., 2010; Alcott et al., 2022; Li et al., 2022). In addition, there is the potential for intense sedimentary Fe cycling [e.g., release of Fe^{2+} to the water column and subsequent re-precipitation of a proportion of this Fe^{2+} as Fe (oxyhydr)oxides] under anoxic ferruginous conditions, resulting in elevated Fe_{HR}/Fe_{T}

ratios combined with low Fe_T/Al (e.g., Li et al., 2022). Thus, while elevated Fe_T/Al ratios provide support for anoxic depositional conditions, lower values should be interpreted with a high degree of caution, particularly when the data contrast with other, more sensitive redox proxies (e.g., Fe speciation, trace metals, biomarkers).

In terms of redox-sensitive trace element proxies, we focus here on Mo and U. Molybdenum is particularly useful since it responds to the availability of dissolved sulfide. Under ferruginous conditions, precipitation of Fe minerals such as Fe (oxyhydr)oxides or green rust (e.g., Zegeye et al., 2012) may draw down Mo through a particulate shuttle mechanism (e.g., Algeo and Tribovillard, 2009; Tribovillard et al., 2012). However, with sufficient sulfide availability under euxinic conditions, the molybdate anion is converted to particle-reactive thiomolybdate (Helz et al., 1996). This commonly results in particularly large Mo enrichments in the sediment (Emerson and Huested, 1991; Helz et al., 1996; Erickson and Helz, 2000). Indeed, the degree of Mo enrichment can help to distinguish permanently euxinic, Mo-replete settings (> 100 ppm), intermittently/seasonally euxinic settings or permanently Mo-depleted euxinic settings (25–100 ppm), and non-euxinic settings (< 25 ppm) (Tribovillard et al., 2006; Scott and Lyons, 2012). Like Mo, U behaves conservatively under oxic water column conditions, but unlike Mo, U reduction primarily occurs in anoxic sediments, without the requirement for free sulfide, and U may therefore be enriched beneath anoxic bottom waters, regardless of whether euxinic or ferruginous conditions dominate (e.g., Klinkhammer and Palmer, 1991; Partin et al., 2013). In addition, Mn–Fe redox cycling near the oxic-anoxic interface can accelerate RSTE enrichments in sediments (Algeo and Tribovillard, 2009).

An upwelling setting can be diagnosed by the combined use of Cd/Mo ratios (> 0.1) and

Co×Mn values (< 0.4) (Sweere et al., 2016), with upwelling strength indicated by Cd-Mo relationships (i.e., using a Cd-Mo crossplot; Sweere et al., 2016; Zhang et al., 2021). Empirical data show that sediments from modern perennial or sustained upwelling settings (e.g., the Peru margin) have higher Cd/Mo ratios than those from seasonal or transient upwelling settings (e.g., the Gulf of California) (Sweere et al., 2016; Zhang et al., 2021). Thus, Cd/Mo ratios of > 0.6, 0.1–0.6, and < 0.1 indicate perennial upwelling, seasonal upwelling, and restricted settings, respectively (Sweere et al., 2016).

5. Results and discussion

5.1 Spatiotemporal variations in redox conditions across the shelf-basin transect

5.1.1 PDS section

In this lower slope section, ratios of Fe_{HR}/Fe_T range from 0.41 to 1.00 (Figs. 3a and 4a), suggesting dominantly anoxic bottom-water conditions (Poulton and Canfield, 2011), which is supported by dominantly high U concentrations and U_{EF} values (Fig. 3a) (Tribovillard and Algeo, 2012; He et al., 2022). Parts of the section also have elevated Fe_T/Al ratios (> 0.66), providing support for anoxic depositional conditions. However, while some Fe_T/Al ratios fall in the typical zone for oxic deposition (0.55 ± 0.11), many samples have highly depleted ratios, which is a common feature throughout the basinal transect (Fig. 3). This clearly highlights the limitations of using Fe_T/Al as a paleoredox proxy. Low Fe_T/Al samples have elevated Fe_{HR}/Fe_T ratios and elevated U_{EF} values, and generally have low Fe_{py}/Fe_{HR} ratios and low Mo_{EF} values, suggesting anoxic-ferruginous depositional conditions. These specific geochemical characteristics are emerging as a common feature of ferruginous conditions (e.g., Poulton et al., 2010; Alcott et al., 2022; Li et al., 2022), and imply intense Fe cycling between the water column and shallow sediments (see above; Li et al., 2022). By contrast, elevated Fe_T/Al ratios commonly coincide with high Fe_{py}/Fe_{HR} ratios and/or high Mo_{EF} values (Fig. 3), implying at least a degree of euxinia, which would trap diagenetically mobilized Fe^{2+} in the sediment as sulfide phases, thus maintaining primary elevated Fe_T/Al ratios arising from water column precipitation of Fe minerals under anoxic conditions (Poulton and Canfield, 2011; Raiswell et al., 2018; Poulton, 2021).

On top of these general geochemical redox characteristics, distinct temporal variability is evident in the evolving redox conditions through the lower slope section (Figs. 3a and 4a-b). In the LPMM, samples with elevated Fe_{py}/Fe_{HR} ratios coincide with relatively low Mo enrichments (Fig. 4b). While these combined characteristics may indicate a possible degree of euxinia (i.e., weak or intermittent), particularly because Fe_T/Al ratios are also elevated (see above) in the upper LPMM (Fig. 3a), the low Mo contents could be caused by limited Mo resupply under relatively weak upwelling conditions (see Section 5.2). For the MCMM, dominantly anoxic-ferruginous conditions are indicated throughout most of the interval, with the possible development of intermittent or weak euxinia towards the top (Figs. 3a and 4a). There is also a zone of elevated Fe_{py}/Fe_{HR} towards the top of the Roadian stage in the MCMM, which coincides with commonly elevated Mo_{EF} values (Fig. 3a). However, these data fall in the particulate shuttle zone on a Mo_{EF} vs U_{EF} crossplot (Fig. 5a), suggesting elevated drawdown of Mo due to uptake by Fe (oxyhydr)oxides under ferruginous conditions (Tribovillard and Algeo, 2012).

In the UMM, there is a peak in Fe_{py}/Fe_{HR} ratios, but this peak falls below the threshold for identification of persistent euxinia (Fig. 3a). Combined with moderate enrichments in Mo, this suggests intermittent euxinia, which progressed to an interval of stronger and more persistent euxinia in the middle of the LSM (Figs. 3a and 4a-b). Enrichments in Fe_{HR}/Fe_T in the MSM, combined with generally low Fe_{py}/Fe_{HR} ratios (Figs. 3a and 4a), and low U_{EF} with moderate Mo_{EF} values (Figs. 3a and 5a), indicates a return to ferruginous conditions, with the progression to lower Fe_{HR}/Fe_T through this interval possibly implying a gradual return to a better ventilated water column in this part of the basin.

5.1.2 GD core

Elevated Fe_{HR}/Fe_T ratios, U concentrations and U_{EF} values persist throughout almost the entirety of the GD core (Fig. 3b), suggesting persistent anoxia (Poulton and Canfield, 2011; Tribovillard and Algeo, 2012; Poulton, 2021). Fe_{py}/Fe_{HR} ratios are high throughout the GD core, implying dominantly euxinic conditions (Figs. 3b and 4c), which in most of the section is supported by elevated Mo_{EF} values (Fig. 3b). However, Mo_{EF} values and Mo concentrations fluctuate considerably, with some samples from the LPMM and MSM possibly indicating ferruginous (or intermittently ferruginous) conditions, based on relationships between Mo concentrations and Fe_{py}/Fe_{HR} ratios (Fig. 4d), as well as Mo_{EF} and U_{EF} values (Fig. 5a). Considerable fluctuations in Mo concentrations through the MCMM, UMM and MSM (Fig. 3b), may indicate that the water column fluctuated between highly and weakly/intermittently euxinic (Scott and Lyons, 2012). However, despite the prevalence of euxinia, Fe_T/Al ratios are often below the normal range for oxic marine sediments (Fig. 3b), although ratios generally do not reach the very lowest levels found under ferruginous conditions in the deeper, slope setting

(Fig. 3a). Since euxinia is more effective at trapping Fe^{2+} in the sediments, relative to the possibility for remobilization back to the water column under ferruginous conditions (Poulton and Canfield, 2011; Poulton, 2021), the prevalence of low Fe_T/Al suggests that the background ratios in detrital sediments delivered to this region were low. Thus, Fe_T/Al ratios across the basin appear to have been affected both by recycling of Fe^{2+} back to the water column in some ferruginous intervals (see above), as well as low detrital values, which reinforces the difficulties inherent in using Fe_T/Al as a reliable paleoredox proxy.

The relatively low Mo concentrations observed in some euxinic sections may provide further insight into paleoenvironmental conditions, since Mo drawdown can also be affected by hydrographic restriction (e.g., McArthur et al., 2008). Generally, the degree of basin restriction is related to eustatic changes, which could have caused significant restriction owing to reduced water depths over sills at the basin margin (Zhang et al., 2020, 2022a, b). A higher degree of restriction during this interval is potentially indicated by low Mo/TOC ratios (Fig. 5b; see Section 5.2), which are similar to those observed in euxinic sediments of restricted basins (e.g., Algeo and Lyons, 2006). Limited resupply of Mo via deep water renewal would have resulted in a reduced local Mo seawater budget, resulting in less uptake of Mo per unit of organic matter compared to fully connected ocean basins (Algeo and Lyons, 2006; McArthur et al., 2008). Thus, persistent euxinia could have gradually drawn down the Mo concentration of seawater, resulting in relatively low Mo concentrations in the euxinic sediments, which is also supported by the relationship between Fe_{py}/Fe_{HR} and Mo (Fig. 4d).

5.1.3 QLS section

High Fe_{HR}/Fe_T ratios (> 0.38) and U_{EF} values occur throughout the QLS section (Fig. 3c), suggesting persistent bottom water anoxia across the outer shelf during the Middle Permian. However, low Fe_{py}/Fe_{HR} ratios coupled with low Mo concentrations and Mo_{EF} values, indicate anoxic-ferruginous conditions during deposition of the LPMM and MCMM (Fig. 3c). Through the UMM, sporadic enrichments in Fe_{py}/Fe_{HR}, Mo concentrations and Mo_{EF} values indicate fluctuations between anoxic ferruginous, weak/intermittent euxinia, and more strongly euxinic conditions, which is consistent with strong fluctuations in Fe_T/Al ratios as discussed above (Figs. 3c and 4e-f). Water column redox conditions continued to fluctuate through the LSM and MSM, with high peaks in Mo coupled with Fe_{py}/Fe_{HR} ratios that fall to below 0.6 after initial high values (Figs. 3c and 4e-f), likely indicating dominantly ferruginous conditions with short-term intervals of euxinia, which is supported by data plotting in the particulate shuttle zone on the U_{EF} vs Mo_{EF} crossplot (Fig. 5a).

5.1.4 Synthesis of the spatiotemporal redox records

The data through our three studied sites document both short-term and longer-term spatio-temporal changes across the Lower Yangtze shelf-basin transect (Fig. 6). The Roadian-Wordian interval (i.e., LPMM–lower UMM) is characterized by laterally variable redox conditions, with euxinia dominating in mid-water depths (shelf margin), and anoxic-ferruginous conditions being more dominant in both deeper (lower slope) and shallower (outer shelf) waters. The early-middle Capitanian stage (i.e., upper UMM–LSM) is marked by more widespread, particularly enhanced euxinia across the shelf-basin transect (Fig. 6). Following the middle Capitanian (i.e., MSM), redox conditions returned to a dominantly anoxic-ferruginous state.

5.2 Hydrographic response to variability in Guadalupian upwelling

Widespread upwelling has been proposed along the Eastern Paleo-Tethys Margin during the Middle Permian (Yao et al. 2015; Shi et al., 2016; Zhang et al., 2018, 2021, 2022a). Our previous studies on both the PDS section and GD core (Fig. 7a-b), combined with new data from the QLS section (Fig. 7c; and see the Supplementary Materials for further discussion), indicate relatively strong upwelling (sometimes seasonal) in the LPMM, MCMM and lower UMM (i.e., Roadian-Wordian), but with a gradual transition from a seasonal upwelling setting to a more restricted environment through the UMM and across the boundary with the LSM (i.e., early-middle Capitanian) (Zhang et al., 2021, 2022a). This may indicate a significant weakening or collapse in the upwelling system (Zhang et al., 2021, 2022a). Following a sea level lowstand, upwelling increased in the upper LSM and MSM (i.e., late Capitanian; Fig. 7). This evolution of the Guadalupian upwelling system along the western Yangtze Platform is supported by Cd vs Mo and Al vs (Co×Mn) crossplots (Fig. 8).

The Mo_{EF}-U_{EF} covariation patterns can be used to help evaluate the degree of hydrographic restriction (e.g., Algeo and Tribovillard, 2009). As shown in Fig. 5a, almost all LPMM samples plot in the unrestricted marine zone. Similarly, most samples of the MCMM and lower UMM have predominantly high Mo_{EF} and U_{EF} values, which mainly scatter around the unrestricted marine trend, but with a few values trending towards the particulate shuttle field (Fig. 5a). This reflects an open marine upwelling system with a weak or intermittently operating shuttle during this time interval. For the upper UMM and LSM, most samples show high Mo_{EF} values relative to U enrichments, defining a covariation pattern that falls between the unrestricted marine trend and the particulate shuttle field (Fig. 5a). This enhanced particulate shuttle is consistent with strong but temporally variable water-mass exchange across this gradually restricted basin. Further up-section, most samples of the MSM cluster close to the area of unrestricted conditions, with low Mo/U ratios (< SW), except for samples of the QLS section that are still dominated by a particulate shuttle influence (Fig. 5a).

Although Mo/TOC ratios in sediments can also provide insight into the degree of water-mass restriction (Algeo and Lyons, 2006; Algeo and Rowe, 2012), this approach is not suitable for continental margin upwelling settings, in which low Mo/TOC ratios (e.g., ~6 ± 3 of modern Namibian shelf, Algeo and Lyons, 2006) are a consequence of redox rather than hydrographic controls (e.g., Algeo and Rowe, 2012). Thus, low Mo/TOC ratios (average 1.66, 3.81 and 8.08 for the PDS section, GD core and QLS section, respectively) observed in the Kuhfeng Formation (Figs 5b and 7) can be attributed to insufficient H_2S build-up due to rapid water mass exchange under the strong upwelling system at this time (e.g., Algeo and Lyons, 2006). By contrast, with the weakening of upwelling, slightly increased Mo/TOC ratios (average 21.96, 10.89 and 35.70 for the PDS section, GD core and QLS section, respectively) during the transition to the Yinping Formation (Figs 5b and 7) likely relate to the abrupt changes in redox conditions (e.g., Algeo and Rowe, 2012), which were a potential response to enhanced restriction.

Taken together, accompanying the changes in upwelling, the observed patterns in our three studied sites show spatially and temporally variable water-mass exchange across the Lower

Yangtze basin. The Roadian-Wordian stage is characterized by laterally unconfined circulation and strong watermass exchange in both deeper and shallower waters, whereas the early-middle Capitanian stage is marked by weakened deeper-water ventilation and enhanced shallow-water restriction, with an effective particulate shuttle.

5.3 Reconstruction and dynamic evolution of an upwelling-driven OMZ-type redox structure

Detailed examination of paleoredox data for our three studied sections provides compelling evidence for strong temporal and spatial variability in marine redox conditions along the Middle Permian Yangtze Platform margin (Figs. 3 and 6). A clear euxinic state is also evident in the Hexian area (Zhang et al., 2019a), located between Nanjing and Chaohu, and the Xiaolao area (Wei et al., 2019), situated between the Gangdi and Chaohu (Figs. 1c-d and 6). Thus, a synthesis of these laterally varying redox conditions points to an upwelling-driven OMZ-type oceanic structure, in which anoxic-ferruginous to euxinic redox conditions dynamically coexisted at intermediate depths (Figs. 6a-e).

The location and dimensions of this “OMZ-type redox structure” appears to have fluctuated: five phases of redox evolution on the eastern margin of the Paleo-Tethys Ocean can be determined (Fig. 6). As the main period of Late Paleozoic Ice Age (LPIA) weakened, the Middle Permian saw the transition to a greenhouse climate (e.g., Chen et al., 2013; Zhang et al., 2021), leading to a wide range of upwelling systems around the world (Beauchamp and Baud, 2002). With rapid transgression during the early Roadian, vigorous upwelling occurred on the Eastern Paleo-Tethys margin (Kametaka et al., 2005; Yao et al., 2015; Zhang et al., 2018, 2021, 2022a), triggering an OMZ (Fig. 6a). This process may have been exacerbated by increased nutrient input driven by enhanced chemical weathering under gradual climate warming (e.g., Zhang et al., 2021). Thus, a fluctuating "euxinic wedge" developed at mid-depths on the north-west shelf margin of South China from this interval.

Until the end of the Wordian stage, anoxic-ferruginous water column conditions were a prevalent feature throughout deposition in both shallow-water shelf and deep-water slope settings, whereas euxinia only occurred at intermediate depths, dominantly on shelf margins (Figs. 6a-b). Strong watermass exchange with unconfined circulation dominated across the basin with the enhanced development of this open marine upwelling system during this interval. Subsequently, marine regression gradually occurred from the early Capitanian stage, as inferred from increased terrestrial inputs, which may have resulted in a weaker connection to the open ocean (Zhang et al., 2020, 2022b). During the early-middle Capitanian, all five sections show parallel evidence for enhanced euxinia, which was coupled to the weakened upwelling and enhanced hydrographic restriction, suggesting an expansion of the OMZ (Fig. 6c). This zone prevailed until the middle Capitanian (i.e., *Jinogondolella xuanhanenis* conodont zone), and the intensified euxinia encroached to a maximum lateral extent to within ~250 km from the paleoshoreline (Fig. 6d). Subsequently, the area of euxinia contracted probably driven by regression (Zhang et al., 2022b), resulting in a less extensive OMZ typified by dominantly ferruginous conditions (Fig. 6e).

5.4 Potential drivers of long-lasting OMZ anoxia and the spread of euxinia

Generally, the dynamics of nutrient cycling and the degree of oxygen depletion are closely linked (e.g., Algeo and Ingall, 2007; Schobben et al., 2020). As a key limiting nutrient for marine productivity, phosphorus (P) is a potential driver for eutrophication-induced oxygen depletion and thus the development of widespread anoxia (e.g., Meyer et al., 2008; Schobben et al., 2020). Here, we consider TOC/TP and P/Al ratios to provide insight into the potential significance of P cycling across the Middle Permian Lower Yangtze Basin (e.g., Algeo and Ingall, 2007), recognizing that the presence of detrital P exerts an added complication to these records (e.g., Guilbaud et al., 2020; Schobben et al., 2020; Qiu et al., 2020).

Extremely low TOC/TP ratios (well below the Redfield ratio of 106:1) combined with relatively high P/Al values in the LPMM (Fig. 7), suggest low recycling of P (e.g., Guilbaud et al., 2020; Schobben et al., 2020). This is consistent with drawdown of P under the dominantly ferruginous conditions envisaged for this interval (Fig. 7), which resulted in the extensive formation of phosphate nodules (e.g., Kametaka et al., 2009; Zhang et al., 2020). Indeed, the formation of phosphate nodules at this time, coupled with high P/Al, suggests a high bioavailable P flux to the basin (either through enhanced chemical weathering or intense upwelling), which may have initiated the development of anoxic conditions (e.g., Schobben et al., 2020; Qiu et al., 2022).

During deposition of the MCMM, TOC/TP ratios increase dramatically, to values greatly in excess of the Redfield ratio, while the P/Al ratios decrease to values below, or approaching, average shale (Fig. 7). This suggests very efficient recycling of P back to the water column during preferential release of P from organic matter during microbial remineralization, coupled with release of P during the reductive dissolution of Fe (oxyhydr)oxides (e.g., Ingall et al., 1993; Ingall and Jahnke, 1997; Slomp et al., 2002; Algeo and Ingall, 2007). Both these processes are stimulated by the production of dissolved sulfide, which is consistent with the enhanced development of euxinia at this time (Fig. 6). Enhanced P recycling, combined with strong watermass mixing under the influence of the perennial upwelling, likely resulted in the rapid transport of bioavailable P into shallower productive waters, further fueling increased productivity and thus the organic flux to the sediments (e.g., Algeo and Ingall, 2007). Overall, efficient recycling of P would have resulted in a positive feedback loop where intensified euxinia was sustained, thereby promoting further P cycling and elevated productivity.

During the UMM, TOC/TP ratios generally decrease, particularly in the more proximal settings (i.e., GD core and QLS section), but values still considerably exceed the Redfield ratio (Fig. 7). This decrease may not be related to lithological change, because no correlation was observed between TOC/TP ratios and Al contents (not shown) suggesting there was no influence of detrital input variations. Large fluctuations of TOC/TP ratios within the same lithological member excludes the possible effect of lithological changes. P/Al ratios also decline over this interval, and these combined observations suggest efficient P recycling back to the water column as euxinic conditions continued to expand (Fig. 6). In addition, enhanced weathering driven by climate warming, as indicated by increased values of chemical index of alteration (i.e., CIA; Zhang et al., 2021, 2022a), likely also promoted an increased influx of P to the coastal area at this time, further enhancing productivity and oxygen consumption in proximal settings (Zhang et al., 2021). This is supported by additional evidence for particularly high rates of productivity at this time from trace element systematics (Zhang et al., 2021).

Sluggish basinal circulation, coupled with rapid climate warming and a gradual collapse in upwelling during this interval, may have further accelerated the spread of euxinic conditions.

Across the LSM, TOC/TP ratios decline, particularly in the deeper water sections, while P/Al ratios show a transient increase (Fig. 7). This implies more efficient trapping of reactive P as authigenic phases (e.g., fluorapatite) during diagenesis, which is supported by the strong positive correlations between Ca and P contents in both the PDS and QLS sections (R^2 = 0.91 and 0.79, respectively; Fig. S2). Changes in the P cycling described above may have been driven by the particularly enhanced development of euxinia at this time (Fig. 6). Expanded euxinia commonly lowers water column sulfate concentrations, which has the effect of enabling more phosphate to be trapped in the sediment as authigenic phases (e.g., Xiong et al., 2019). It is noteworthy that the drawdown of recycled P mainly occurred in the proximal (i.e., QLS section) and distal settings (i.e., PDS section) (Fig. 7), indicating a strong redox-controlled nutrient shuttle (e.g., Schobben et al., 2020), operating from the heart of the euxinic zone in the GD core, across the shelf-basin transect (Fig. 6). As sea level dropped to its lowstand during MSM deposition, the OMZ declined in extent and conditions were dominantly ferruginous, restricting P recycling and productivity. This effectively constrained the maximum spatial extent and intensity of anoxia.

5.5 Impact of widespread anoxia-euxinia on the mid-Capitanian biotic crisis

5.5.1 Global redox links to OMZ expansion in the Lower Yangtze basin

The widespread anoxic conditions across the Lower Yangtze basin during the early-middle Capitanian support an expansion and intensification of an OMZ, which ultimately increased the frequency of sulfidic water incursions onto the shelf. This OMZ expansion also likely occurred in the Middle (e.g., Tianfengping and Maocaojie sections; Shi et al., 2016; Wei et al., 2016) and Upper (e.g., Chaotian section, Saitoh et al., 2014) Yangtze area during the early-middle Capitanian (Fig. 9), indicating extensive anoxic/euxinic conditions developed along the eastern Paleo-Tethys ocean margin. Elsewhere, the southeast Yangtze Platform margin (e.g., the Penglaitan section), which faced the western edge of Panthalassa, also shows evidence for long-term dysoxic to anoxic conditions in the early-middle Capitanian (from the *J. altudaensis* to *J. xuanhanenis* conodont zones; Wei et al., 2016; Song et al., 2023), with the development of euxinia at the end of Capitanian (Fig. 9; Zhang et al., 2015; Wei et al., 2016; Song et al., 2023). Also, the northern and western margins of Pangea (e.g., Opal Creek and Boreal Realm sections), which were located in the western upwelling zone of the Panthalassic ocean, exhibited an intensification of oxygen depletion, or even euxinic conditions, in the middle to late Capitanian (Fig. 9; e.g., Schoepfer et al., 2013; Zhang et al., 2015; Bond et al., 2015, 2020; Smith et al., 2020). Unlike these continental shelf margin settings, the abyssal mid-Panthalassa (e.g., Gujo-Hachiman section) was dominated by oxic conditions (Fujisaki et al., 2019), but also appears to have experienced suboxic conditions in the late Capitanian (Fig. 9; Onoue et al., 2021). Therefore, taking into account the widespread development of strong upwelling related to vigorous global-ocean circulation during the Middle Permian (e.g., Beauchamp and Baud, 2002), these records indicate that intensified anoxic to euxinic conditions mainly occurred in continental shelf margin settings, and were hence related to OMZ expansion during the middle Capitanian. Accompanied by global regression, the OMZ would have allowed encroachment of sulfidic waters onto the continental shelves until the end of the Capitanian.

5.5.2 Effect of anoxia-euxinia on the mid-Capitanian biotic crisis

From the Roadian to Wordian stages, the dynamic euxinic water mass that developed along the shelf margin likely placed a major constraint on communities living in deeper-water and ocean-facing habitats, and thus likely accounts for the loss or turnover of radiolarians (e.g., *Pseudoalbaillella*) and sponge spicules (e.g., Zhang et al., 2019b). During the early-middle Capitanian, intensified mid-depth euxinic waters coupled with the OMZ expansion, resulted in the spread of anoxia into previously oxygenated areas of the shelf, progressively restricting habitable shallower shelf habitats (e.g., Clapham et al., 2009). This incursion during the middle Capitanian would have created widespread inhospitable conditions for benthic shelf communities leading to the observed gradual decrease in marine invertebrate diversity (e.g., rugose corals; Fig. 9) (e.g., Clapham et al., 2009; Shen and Shi, 2009; Song et al., 2023). Rapid sea level drop accompanied by the eruption of ELIP could compress their habitat range along the continental margins (e.g., Wei et al., 2016), further stressing benthic communities (Fig. 9), despite some areas (e.g., the Laibin area) also showed the recovery of benthic faunas during this interval (e.g., Kaiho et al., 2005; Chen et al., 2009; Huang et al., 2019). In combination with these ecological stresses, the development of widespread anoxia-euxinia around the world during the end-Capitanian likely led to significant selective taxonomic loss of genera, eventually driving some benthic and even nektonic fauna to extinction (Fig. 9).

6. Conclusions

In order to unravel the redox history of eastern Paleo-Tethys Ocean (South China) during the Middle Permian, and to decipher possible influences on the mid-Capitanian biotic crisis, we evaluated Fe speciation, redox-sensitive trace metals systematics, and P cycling for three different water-depth sections/cores across a shelf-to-basin transect in the Lower Yangtze region. Our results provide compelling evidence for strong temporal and spatial variability in marine redox conditions along the Yangtze Platform margin. A synthesis of these varying marine redox conditions points to an OMZ-type setting, in which euxinic waters dynamically coexisted at intermediate depths, with commonly ferruginous deeper waters. We construct a five-phase spatiotemporal evolution of redox conditions. Vigorous upwelling in the Roadian-Wordian lead to the development of an OMZ on the continental margin dominated by anoxic-ferrugonous conditions in unrestricted setting. The intensity of upwelling declined in the Capitanian and yet the OMZ expanded, with euxinia becoming more important. Enhanced phosphorus cycling across the basin could be a potential driver of the Guadalupian long-lasting OMZ anoxia and subsequent spread of euxinia during the Capitanian. During the Capitanian, ocean circulation and upwelling declined enhancing restriction which, together with increased terrestrial nutrient supply, caused intensification of euxinic conditions in marginal shelf seas. The spread and shallowing of the euxinic waters coincided with the mid-Capitanian biotic crisis, suggesting these redox changes were a key driving mechanism.

Acknowledgements

We thank Dr. Gang Shi for providing samples and Dr. Biao Liu for assistance in the fieldwork. Prof. Shuzhong Shen and Dr. Zhong Han is especially acknowledged for their helpful and constructive suggestions. Funding was provided by the National Natural Science Foundation of China (Grant Nos. 42202130, 41888101 and 42072152). We acknowledge Prof.

Yadong Sun and one anonymous reviewer for their comments that substantially improved this work, as well as Prof. Maoyan Zhu for editorial handling.

References

Alcott, L.J., Krause, A.J., Hammarlund, E.U., Bjerrum, C.J., Scholz, F., Xiong, Y., Hobson, A.J., Neve, L., Mills, B.J.W., März, C., Schnetger, B., Bekker, A., Poulton, S. W., 2020. Development of iron speciation reference materials for palaeoredox analysis. Geostand. Geoanal. Res. 44, 581–591.

Alcott, L.J., Mills, B.J.W., Bekker, A., Poulton, S. W., 2022. Earth's Great Oxidation Event facilitated by the rise of sedimentary phosphorus recycling. Nat. Geosci. 15, 210–216.

Algeo, T.J., Ingall, E., 2007. Sedimentary C_{org}: P ratios, paleocean ventilation, and Phanerozoic atmospheric pO_2. Palaeogeogr. Palaeoclimatol. Palaeoecol. 256, 130–155.

Algeo, T.J., Lyons, T., 2006. Mo-total organic carbon covariation in modern anoxic marine environments: Implications for analysis of paleoredox and paleohydrographic conditions. Paleoceanography 21, PA1016.

Algeo, T.J., Rowe, H., 2012. Paleoceanographic applications of trace-metal concentration data. Chem. Geol. 324, 6–18.

Algeo, T.J., Tribovillard, N., 2009. Environmental analysis of paleoceanographic systems based on molybdenum-uranium covariation. Chem. Geol. 268, 211–225.

Beauchamp, B., Baud, A., 2002. Growth and demise of Permian biogenic chert along northwest Pangea: evidence for end-Permian collapse of thermohaline circulation. Palaeogeogr. Palaeoclimatol. Palaeoecol. 184, 37–63.

Bond, D.P.G., Hilton, J., Wignall, P.B., Ali, J.R., Stevens, L.G., Sun, Y., Lai, X., 2010. The Middle Permian

(Capitanian) mass extinction on land and in the oceans. Earth Sci. Rev. 102, 100–116.

Bond, D.P.G., Wignall, P.B., Joachimski, M.M., Sun, Y., Savov, I., Grasby, S.E., Beauchamp, B., Blomeier, D.P.G., 2015. An abrupt extinction in the Middle Permian (Capitanian) of the Boreal Realm (Spitsbergen) and its link to anoxia and acidification. Geol. Soc. Am. Bull. 127, 1411–1421.

Bond, D.P.G., Wignall, P.B., Grasby, S.E., 2020. The Capitanian (Guadalupian, Middle Permian) mass extinction in NW Pangea (Borup Fiord, Arctic Canada): A global crisis driven by volcanism and anoxia. Geol. Soc. Am. Bull. 132, 931–942.

Canfield, D.E., Raiswell, R., Westrich, J.T., Reaves, C.M., Berner, R.A., 1986. The use of chromium reduction in the analysis of reduced inorganic sulfur in sediments and shales. Chem. Geol. 54, 149–155.

Chen, B., Joachimski, M.M., Sun, Y.D., Shen, S.Z., Lai, X.L., 2011. Carbon and conodont apatite oxygen isotope records of Guadalupian-Lopingian boundary sections: climatic or sea-level signal? Palaeogeogr. Palaeoclimatol. Palaeoecol. 311, 145–153.

Chen, B., Joachimski, M.M., Shen, S.Z., Lambert, L.L., Lai, X.L., Wang, X.D., Chen, J., Yuan, D.X., 2013. Permian ice volume and palaeoclimate history: oxygen isotope proxies revisited. Gondwana Res. 24, 77–89.

Chen, Z.Q., George, A.D., Yang, W.R., 2009. Effects of middle-late Permian sea-level changes and mass extinction on the formation of the Tieqiao skeletal mound in the Laibin area, South China. Aust. J. Earth Sci. 56, 745–763.

Clapham, M.E., Shen, S.Z., Bottjer, D.J., 2009. The double mass extinction revisited: reassessing the severity, selectivity, and causes of the end-Guadalupian biotic crisis (Late Permian). Paleobiology 35, 32–50.

Clarkson, M.O., Poulton, S.W., Guilbaud, R., Wood, R.A., 2014. Assessing the utility of Fe/Al and Fe-speciation to record water column redox conditions in carbonate-rich sediments. Chem. Geol. 382, 111–

122.
Emerson, S.R., Huested, S.S., 1991. Ocean anoxia and the concentrations of molybdenum and vanadium in seawater. Mar. Chem. 34 (3-4), 177–196.
Erickson, B.E., Helz, G.R., 2000. Molybdenum (VI) speciation in sulfidic waters: Stability and lability of thiomolybdates. Geochim. Cosmochim. Acta 64 (7), 1149–1158
Fujisaki, W., Sawaki, Y., Matsui, Y., Yamamoto, S., Isozaki, Y., Maruyama, S., 2019. Redox condition and nitrogen cycle in the Permian deep mid-ocean: A possible contrast between Panthalassa and Tethys. Glob. Planet. Chang. 172, 179–199.
Golonka, J., Ross, M.I., Scotese, C.R., 1994. Phanerozoic paleogeographic and paleoclimatic modeling maps. In: Embry, A.F., Beauchamp, B., Glass, D.J. (Eds.), Pangea: Global Environments and Resources. Canadian Society of Petroleum Geology Memoir, 17, pp. 1–47.
Guilbaud, R., Poulton, S.W., Thompson, J., Husband, K.F., Zhu, M., Zhou, Y., Shields, G. A., Lenton, T.M., 2020. Phosphorus-limited conditions in the early Neoproterozoic ocean maintained low levels of atmospheric oxygen. Nat. Geosci. 13, 236–301.
He, T., Wignall, P.B., Newton, R.J., Atkinson, J.W., Keeling, J.F.J., Xiong, Y., Poulton, S.W., 2022. Extensive marine anoxia in the European epicontinental sea during the end-Triassic mass extinction. Glob. Planet. Chang. 210, 103771.
He, W., Wu, S., Zhang, K., Pu, J., 1999. Classification of radiolarian fossil zones and environmental analysis of Gufeng Formation in Lower Yangtze region. Jiangsu Geol 23, 17–23 (in Chinese with English abstract).
Helz, G.R., Miller, C.V., Charnock, J.M., Mosselmans, J.F.W., Pattrick, R.A.D., Garner, C. D., Vaughan, D.J., 1996. Mechanism of molybdenum removal from the sea and its concentration in black shales: EXAFS

evidence. Geochim. Cosmochim. Acta 60, 3631–3642.

Huang, Y.G., Chen, Z.Q., Wignall, P.B., Grasby, S., Zhao, L.S., Wang, X.D., Kaiho, K., 2019. Biotic responses to volatile volcanism and environmental stresses over the Guadalupian-Lopingian (Permian) transition. Geology 47, 175–178.

Ingall E., Jahnke R., 1997. Influence of water-column anoxia on the elemental fractionation of carbon and phosphorus during sediment diagenesis. Mar. Geol. 139, 219–229.

Ingall E. D., Bustin R. M., Van Cappellen P., 1993. Influence of water column anoxia on the burial and preservation of carbon and phosphorus in marine shales. Geochim. Cosmochim. Acta 57, 303–316.

Isozaki, Y., Kawahata, H., Ota, A., 2007. A unique carbon isotope record across the Guadalupian-Lopingian (Middle-Upper Permian) boundary in mid-oceanic paleo-atoll carbonates: the high-productivity "Kamura event" and its collapse in Panthalassa. Glob. Planet. Chang. 55, 21–38.

Jin, Y., Zhang, J., Shang, Q., 1994. Two phases of the end-Permian mass extinction. Can. Soc. Petrol. Geol. 17, 813–822.

Kaiho, K., Chen, Z.Q., Ohashi, T., Arinobu, T., Sawada, K., Cramer, B.S., 2005. A negative carbon isotope anomaly associated with the earliest Lopingian (Late Permian) mass extinction. Palaeogeogr. Palaeoclimatol. Palaeoecol. 223, 172–180.

Kaiho, K., Grasby, S.E., Chen, Z.-Q., 2023. High-temperature combustion event spanning the Guadalupian−Lopingian boundary terminated by soil erosion. Palaeogeogr. Palaeoclimatol. Palaeoecol. 618, 1–11.

Kametaka, M., Nagai, H., Zhu, S., Takebe, M., 2009. Middle Permian radiolarians from Anmenkou, Chaohu, Northeastern Yangtze platform, China. Island Arc 18, 108–125.

Kametaka, M., Takebe, M., Nagai, H., Zhu, S., Takayanagi, Y., 2005. Sedimentary environments of the

Middle Permian phosphorite-chert complex from the northeastern Yangtze platform, China; the Kuhfeng Formation: a continental shelf radiolarian chert. Sediment. Geol. 174, 197–222.

Klinkhammer, G., Palmer, M.R., 1991. Uranium in the oceans: where it goes and why. Geochim. Cosmochim. Acta 55, 1799–1806.

Li, S., Wignall, P.B., Poulton, S.W., Hedhli, M., Grasby, S.E., 2022. Carbonate shutdown, phosphogenesis and the variable style of marine anoxia in the late Famennian (Late Devonian) in western Laurentia. Palaeogeogr. Palaeoclimatol. Palaeoecol. 589, 110835.

Lv, B.Q., Zhai, J.Z., 1990. Sedimentation of anoxic environments under transgression and upwelling process in Early Permian in Lower Yangtze area. China Sci. Bull. 35, 1193–1198.

Lv, B.Q., Cai, J.G., Liu, F., Shao, L., Wang, H.G., Quan, Q.S., 2010. Upwelling deposits at the marginal slope of a carbonate platform in Qixia stage and its relation with hydrocarbon source rocks. Marine Geol. Quat. Geol. 30, 109–118 (in Chinese with English abstract).

Lyons, T.W., Severmann, S., 2006. A critical look at iron paleoredox proxies: new insights from modern euxinic marine basins. Geochim. Cosmochim. Acta 70, 5698–722.

McArthur, J.M., Algeo, T.J., Van de Schootbrugge, B., Li, Q., Howarth, R.J., 2008. Basinal restriction, black shales, Re-Os dating, and the Early Toarcian (Jurassic) oceanic anoxic event. Paleoceanography 23, PA4217.

Meyer, K.M., Kump, L.R., Ridgwell, A., 2008. Biogeochemical controls on photic-zone euxinia during the end-Permian mass extinction. Geology 36, 747–750.

Onoue, T., Soda, K., Isozaki, Y., 2021. Development of deep-sea anoxia in Panthalassa during the Lopingian (Late Permian): insights from redox-sensitive elements and multivariate analysis. Front. Earth Sci. 8, 613126.

Partin, C.A., Bekker, A., Planavsky, N.J., Scott, C.T., Gill, B.C., Li, C., Podkovyrov, V., Maslov, A., Konhauser, K.O., Lalonde, S.V., Love, G.D., Poulton, S.W., Lyons, T.W., 2013. Large-scale fluctuations in Precambrian atmospheric and oceanic oxygen levels from the record of U in shales. Earth Planet. Sci. Lett. 369-370, 284–293.

Poulton, S.W., Canfield, D.E., 2005. Development of a sequential extraction procedure for iron: implications for iron partitioning in continentally derived particulates. Chem. Geol. 214, 209–221

Poulton, S.W., Canfield, D.E., 2011. Ferruginous conditions: a dominant feature of the ocean through earth's history. Elements 7, 107–112.

Poulton, S.W., Fralick, P.W., Canfield, D.E., 2010. Spatial variability in oceanic redox structure 1.8 billion years ago. Nat. Geosci. 3, 486–490.

Poulton, S.W., 2021. The Iron Speciation Paleoredox Proxy. Cambridge Univ. Press pp. 1–20.

Qiu, Z., Zou, C., Mills, B.J.W., Xiong, Y., Tao, H., Lu., B., Liu., H., Xiao., W., Poulton, S.W., 2022. A nutrient control on expanded anoxia and global cooling during the Late Ordovician mass extinction. Commun. Earth Environment, 3, 82.

Raiswell, R., Hardisty, D.S., Lyons, T.W., Canfield, D.E., Owens, J.D., Planavsky, N.J., Poulton, S.W., Reinhard, C.T., 2018. The iron paleoredox proxies: A guide to the pitfalls, problems and proper practice. Am. J. Sci. 318, 491–526.

Saitoh, M., Ueno, Y., Isozaki, Y., Nishizawa, M., Shozugawa, K., Kawamura, T., Yao, J.X., Ji, Z.S., Takai, K., Yoshida, N., Matsuo, M., 2014. Isotopic evidence for water-column denitrification and sulfate reduction at the end-Guadalupian (Middle Permian). Glob. Planet. Chang. 123, 110–120.

Schobben, M., Foster, W.J., Sleveland, A.R.N., Zuchuat, V., Svensen, H.H., Planke, S., Bond, D.P.G., Marcelis, F., Newton, R.J., Wignall, P.B., Poulton, S.W., 2020. A nutrient control on marine anoxia during the end-Permian mass extinction. Nat. Geosci. 13, 640–646.

Schoepfer, S.D.,Henderson, C.M., Garrison, G.H., Foriel, J., Ward, P.D., Selby, D., Hower, J.C., Algeo, T.J., Shen, Y., 2013. Termination of a continent-margin upwelling system at the Permian-Triassic boundary (Opal Creek, Alberta, Canada). Glob. Planet. Chang. 105, 21–35.

Scholz, F., 2018. Identifying oxygen minimum zone-type biogeochemical cycling in Earth history using inorganic geochemical proxies. Earth Sci. Rev. 184, 29–45.

Scott, C., Lyons, T.W., 2012. Contrasting molybdenum cycling and isotopic properties in euxinic versus non-euxinic sediments and sedimentary rocks: refining the paleoproxies. Chem. Geol. 324–325, 19–27.

Shen, S.Z., Shi, G.R., 2009. Latest Guadalupian brachiopods from the Guadalupian/Lopingian boundary GSSP section at Penglaitan in Laibin, Guangxi, South China and implications for the timing of the pre-Lopingian crisis. Palaeoworld 18, 152–161.

Shen, S.Z., Yuan, D.X., Henderson, C.M., Wu, Q., Zhang, Y.C., Zhang, H., Mu, L., Ramezani, J., Wang, X.D., Lambert, L.L., Erwin, D.H., Hearst, J.M., Xiang, L., Chen, B., Fan, J.X., Wang, Y., Wang, W.Q., Qi, Y.P., Chen, J., Qie, W.K., Wang, T.T., 2020. Progress, problems and prospects: an overview of the guadalupian series of South China and North America. Earth Sci. Rev. 211, 103412.

Shi, L., Feng, Q.L., Shen, J., Ito, T., Chen, Z.Q., 2016. Proliferation of shallow-water radiolarians coinciding with enhanced oceanic productivity in reducing conditions during the Middle Permian, South China: evidence from the Kuhfeng Formation of western Hubei Province. Palaeogeogr. Palaeoclimatol. Palaeoecol. 444, 1–14.

Slomp, C.P., Thompson, J., de Lange, G.J., 2002. Enhanced regeneration of phosphorus during formation of the most recent eastern Mediterranean sapropel (S1). Geochim. Cosmochim. Acta 66, 1171–1184.

Smith, P.B., Larson, T., Martindale, C.T., Kerans, C., 2020. Impacts of basin restriction on geochemistry and extinction patterns: A case from the Guadalupian Delaware Basin, USA. Earth Planet. Sci. Lett. 530, 115876.

Song, H.Y., Algeo, T.J., Song, H.J., Tong, J.N., Wignall, P.B., Bond, D.P.G., Zheng, W., Chen, X.M., Romaniello, S.J., Wei, H.Y., Anbar, A.D., 2023. Global oceanic anoxia linked with the Capitanian (Middle Permian) marine mass extinction. Earth Planet. Sci. Lett. 610, 118128.

Stanley, S.M. 2016. Estimates of the magnitudes of major marine mass extinctions in earth history. Proc. Natl. Acad. Sci. U.S.A. 113, E6325–E6334.

Stramma, L., Johnson, G. C., Sprintall, J., Mohrholz, V., 2008. Expanding oxygen-minimum zones in the tropical oceans. Science 320, 655–658.

Sun, Y., Lai, X., Wignall, P.B., Widdowson, M., Ali, J.R., Jiang, H., Wang, W., Yan, C., Bond, D.P.G., Vedrine, S., 2010. Dating the onset and nature of the Middle Permian Emeishan large igneous province eruptions in SW China using conodont biostratigraphy and its bearing on mantle plume uplift models. Lithos 119, 20–33.

Sweere, T., van den Boorn, S., Dickson, A.J., Reichart, G.J., 2016. Definition of new trace-metal proxies for the controls on organic matter enrichment in marine sediments based on Mn, Co, Mo and Cd concentrations. Chem. Geol. 441, 235–245.

Tribovillard, N., Algeo, T.J., Lyons, T., Riboulleau, A., 2006. Trace metals as paleoredox and paleoproductivity proxies: An update. Chem. Geol. 232, 12–32.

Tribovillard, N., Algeo, T.J., Baudin, F., Riboulleau, A., 2012. Analysis of marine environmental conditions based onmolybdenum-uranium covariation - applications to Mesozoic paleoceanography. Chem. Geol. 324–325, 46–58.

Wang, J., Jin, Y.G., 2000. Permian palaeogeographic evolution of the Jiangnan Basin, South China.

Palaeogeogr. Palaeoclimatol. Palaeoecol. 160, 35–44.

Wei, H.Y., Wei, X.M., Qiu, Z., Song, H.Y., Shi, G., 2016. Redox conditions across the G-L boundary in South China: evidence from pyrite morphology and sulfur isotopic compositions. Chem. Geol. 440, 1–14.

Wei, H.Y., Tang, Z.W., Yan, D.T., Wang, J.G., Roberts, A.P., 2019. Guadalupian (Middle Permian) ocean redox evolution in South China and its implications for mass extinction. Chem. Geol. 530, 119318.

Wignall, P.B., 2015. The worst of times: how life on Earth survived eighty million years of extinctions. Princeton University Press.

Wignall, P.B., Sun, Y.D., Bond, D.P.G., Izon, G., Newton, R.J., Vedrine, S., Widdowson, M., Ali, J.R., Lai, X.L., Jiang, H.S., Cope, H., Bottrell, S.H., 2009. Volcanism, mass extinction, and carbon isotope fluctuations in the Middle Permian of China. Science 324, 1179–1182.

Winguth, A.M.E., Heinze, C., Kutzbach, J.E., Maier-Reimer, E., Mikolajewicz, U., Rowley, D., Rees, A., Ziegler, A.M., 2002. Simulated warm polar currents during the middle Permian. Paleoceanography 17, 9-1–9-18.

Wu, Q., Ramezani, J., Zhang, H., Wang, T.T., Yuan, D.X., Mu, L., Zhang, Y.C., Li, X.H., Shen, S.Z., 2017. Calibrating the Guadalupian Series (Middle Permian) of South China. Palaeogeogr. Palaeoclimatol. Palaeoecol. 466, 361–372.

Wu, Q., 2020. High-precision zircon U-Pb geochronological studies of the Permian ash beds from China and North America (Ph.D. Thesis). Univ. of Sci. and Technol. of China pp. 25–46 (in Chinese with English abstract).

Xiong, Y. J., Guilbaud, R., Peacock, C. L., Cox, R. P., Canfield, D. E., Krom, M. D., Poulton, S. W., 2019. Phosphorus cycling in Lake Cadagno, Switzerland: A low sulfate euxinic ocean analogue. Geochim.

Cosmochim. Acta 251, 116–135.

Yao, X., Zhou, Y.Q., Hinnov, L.A., 2015. Astronomical forcing of a Middle Permian chert sequence in Chaohu, South China. Earth Planet. Sci. Lett. 422, 206–221.

Zegeye A., Bonneville S., Benning L. G., Sturm A., Fowle D. A., Jones C. A., Canfield D. E., Ruby C., MacLean L. C., Nomosatryo S., Crowe S. A. and Poulton S. W., 2012. Green rust formation controls nutrient availability in a ferruginous water column. Geology 40, 599–602.

Zhang, B., Yao, S., Wignall, P., Hu, W., Ding, H., Liu, B., Ren, Y., 2018. Widespread coastal upwelling along the Eastern Paleo-Tethys Margin (South China) during the Middle Permian (Guadalupian): Implications for organic matter accumulation. Mar. Pet. Geol. 97, 113–126.

Zhang, B., Yao, S., Hu, W., Ding, H., Liu, B., Ren, Y., 2019a. Development of a high-productivity and anoxic-euxinic condition during the late Guadalupian in the Lower Yangtze region: Implications for the mid-Capitanian extinction event. Palaeogeogr. Palaeoclimatol. Palaeoecol. 531, 108630.

Zhang, B., Yao, S., Wignall, P. B., Hu, W., Liu, B., Ren, Y., 2019b. New timing and geochemical constraints on the Capitanian (Middle Permian) extinction and environmental changes in deep-water settings: Evidence from the Lower Yangtze region of South China. J. Geol. Soc. 176, 588–608.

Zhang, B., Yao, S., Mills, B.J.W., Wignall, P. B., Hu, W., Liu, B., Ren, Y., Li, L., 2020. Middle Permian organic carbon isotope stratigraphy and the origin of the Kamura Event. Gondwana Res. 79, 217–232.

Zhang, B., Wignall, P. B., Yao, S., Hu, W., Liu, B., 2021. Collapsed upwelling and intensified euxinia in response to climate warming during the Capitanian (Middle Permian) mass extinction. Gondwana Res. 89, 31–46.

Zhang B., Yao, S., Hu, W., Han, Z., Liao, Z., Liu, B., Lan, M., 2022a. Middle Permian palaeoclimatic-palaeoceanographic evolution and its controls on organic matter accumulation in the Lower Yangtze upwelling region. Int. J. Coal Geol. 264, 104132.

Zhang, B., Yao, S., Ma, A., Hu, W., Liu, B., Yang, W., 2022b. New geochemical constraints on the development of active continental margin in Southeast China during the Middle Permian and its tectonic implications. Gondwana Res. 103, 458–472.

Zhang, B., Cao, J., Mu, L., Yao, S., Hu, W., Huang, H., Lang, X., Liao, Z., 2023. The Permian Chert Event in South China: New geochemical constraints and global implications. Earth Sci. Rev. 244, 104513.

Zhang, G.J., Zhang, X.L., Li, D.D., Farquhar, J., Shen, S.Z., Chen, X.Y., Shen, Y.A., 2015. Widespread shoaling of sulfidic waters linked to the end-Guadalupian (Permian) mass extinction. Geology 43, 1091–1094.

Zou, C.N., Qiu, Z., Poulton, S.W., Dong, D.Z., Wang, H.Y., Chen, D.Z., Lu, B., Shi, Z.S., Tao, H.F., 2018. Ocean euxinia and climate change “double whammy” drove the Late Ordovician mass extinction. Geology 46, 535–538.

FIGURE CAPTIONS

Fig. 1. (a) Late Guadalupian global paleogeography. Base map from Ron Blakey (http://cpgeosystems.com). (b) Late Guadalupian paleogeographic reconstruction of South China (modified from Yao et al., 2015 and Zhang et al., 2022b). (c) Late Guadalupian paleogeographic reconstruction of the Lower Yangtze area showing section/core localities (red stars). (d–e) Schematic basin cross-section for the Roadian-Wordian and Capitanian Lower Yangtze area, showing the sedimentary facies and relative position of studied sections. Yellow dots and stars indicate sections with redox records from the literature. Abbreviations: PDS = Pingdingshan section, GD = Gangdi core, QLS = Qinglongshan section, HX = Hexian core, XL = Xiaolao, TFP = Tianfengping, MCJ = Maocaojie, CT = Chaotian, TQ = Tieqiao, PLT = Penglaitan, BF = Borup Fiord, BR = Boreal Realm, OC = Opal Creak, DW = Delware, WT = West Texas, FWB = fair-weather wave base.

Fig.2. Middle Permian lithology and $\delta^{13}C_{org}$ chemostratigraphic stratigraphy of the Kuhfeng and Lower Yinping Formation in the Lower Yangtze region (modified from Zhang et al., 2020). The geological timescale is based on Yao et al. (2015), Wu et al. (2017), Zhang et al. (2020), Shen et al. (2020), and Wu (2020). The change in relative water depth is modified from Zhang et al. (2022b). The CA-ID-TIMS U-Pb age of PDS-5 is from Wu (2020). Abbreviations: LPMM = Lower Phosphate Nodule-bearing Mudstone Member, MCMM = Middle Chert-Mudstone Member, UMM = Upper Mudstone Member, LSM = Lower Shale Member, MSM = Middle Shale Member, USM = Upper Shale Member, LSSM = Lower Siltstone-Sandstone Member, S.E. = sedimentary environment, SP = shallow-water ramp, OS = outer shelf, US =

upper slope, MS = middle slope, LS = lower slope, BS= basin, CS = coastal setting.

Fig. 3. Redox proxy data for the PDS section (a), GD core (b), and QLS section (c). Green dashed lines indicate the boundary between the Kuhfeng and Yinping formations, and red dashed lines indicate diagnostic thresholds for different redox conditions (after Lyons and Severmann, 2006; Poulton and Canfield, 2011; Scott and Lyons, 2012; Poulton, 2021). Abbreviations: Fm. = Formation.

Fig. 4. Crossplots of Fe_{py}/Fe_{HR} vs Fe_{HR}/Fe_{T}, and Mo vs Fe_{py}/Fe_{HR} for the PDS section (a–b), GD core (c–d) and QLS section (e–f). Abbreviations: Fm. = Formation.

Fig. 5. Crossplots of Mo_{EF} vs U_{EF} (a), and Mo vs TOC (b) for the three studied sections. The average Mo/U weight ratio of seawater is 3.1 (the Mo/U molar ratio is 7.5–7.9; Algeo and Tribovillard, 2009). Abbreviations: Fm. = Formation.

Fig. 6. Conceptual model for the spatiotemporal evolution of redox conditions along the studied shelf-to-basin transect. The redox records of HX and XL are from Zhang et al. (2019a) and Wei et al. (2019), respectively. Abbreviations: Ser. = Series, Stg. = Stage, Fm. = Formation, *Sw. han.* = *Sweetognathus Hanzhongensis*, *P. longl.* – *P. fus.* = *Pseudoalbaillella longtanesis* – *Pseudoalbaillella fusiformis*, *F. schol.* – *R. uralicus* = *Follicucullus scholasticus* – *Ruzhencevispongus uralicus*, *J. posts.* – *J. altuda.* = *Jinogondolella postserrat* – *Jinogondolella altudaensis*, *J. prexua.* – *J. xuan.* = *Jinogondolella prexuanhanensis* – *Jinogondolella*

xuanhanensis, *J. granti – C. postbi = Jinogondolella granti – Clarkina postbitteri.*

Fig. 7. Stratigraphic variations in the PDS section (a), GD core (b) and QLS section (c) for Cd/Mo, Co×Mn, Mo/TOC, P/Al, and TOC/TP (molar) ratios. The green dashed lines indicate the boundary of Kuhfeng and Yinping Formation, and the red dashed lines represent diagnostic thresholds for proxies of upwelling (after Sweere et al., 2016) and P cycling (after Algeo and Ingall, 2007; Schobben et al., 2020). Data of PDS section and GD core are from Zhang et al., 2021, 2022a.

Fig. 8. Crossplots of Cd vs Mo (a), Co×Mn vs Al (b) for the three studied sections. These basic graphs are modified from Sweere et al. (2016).

Fig. 9. Compilation of global redox records in the context of the Capitanian marine biotic crisis and contemporaneous events. The redox records are from Schoepfer et al., 2013 (OC), Saitoh et al., 2014 (CT), Bond et al., 2015, 2020 (BR and BF), Zhang et al., 2015 (WT and TQ), Shi et al. 2016 (MCJ), Wei et al., 2016, 2019 (PLT, TFP, and XL), Fujisaki et al., 2019 (SW Japan), Zhang et al., 2019a (HX), and Smith et al., 2020 (DW). The paleontological data are summarized from Shen and Shi (2009) and Bond et al. (2010). Events shown are the Emeishan LIP (Wignall et al., 2009), climate warming (Zhang et al., 2021), and regression (Sun et al., 2010; Zhang et al., 2019b).

Fig. 1.

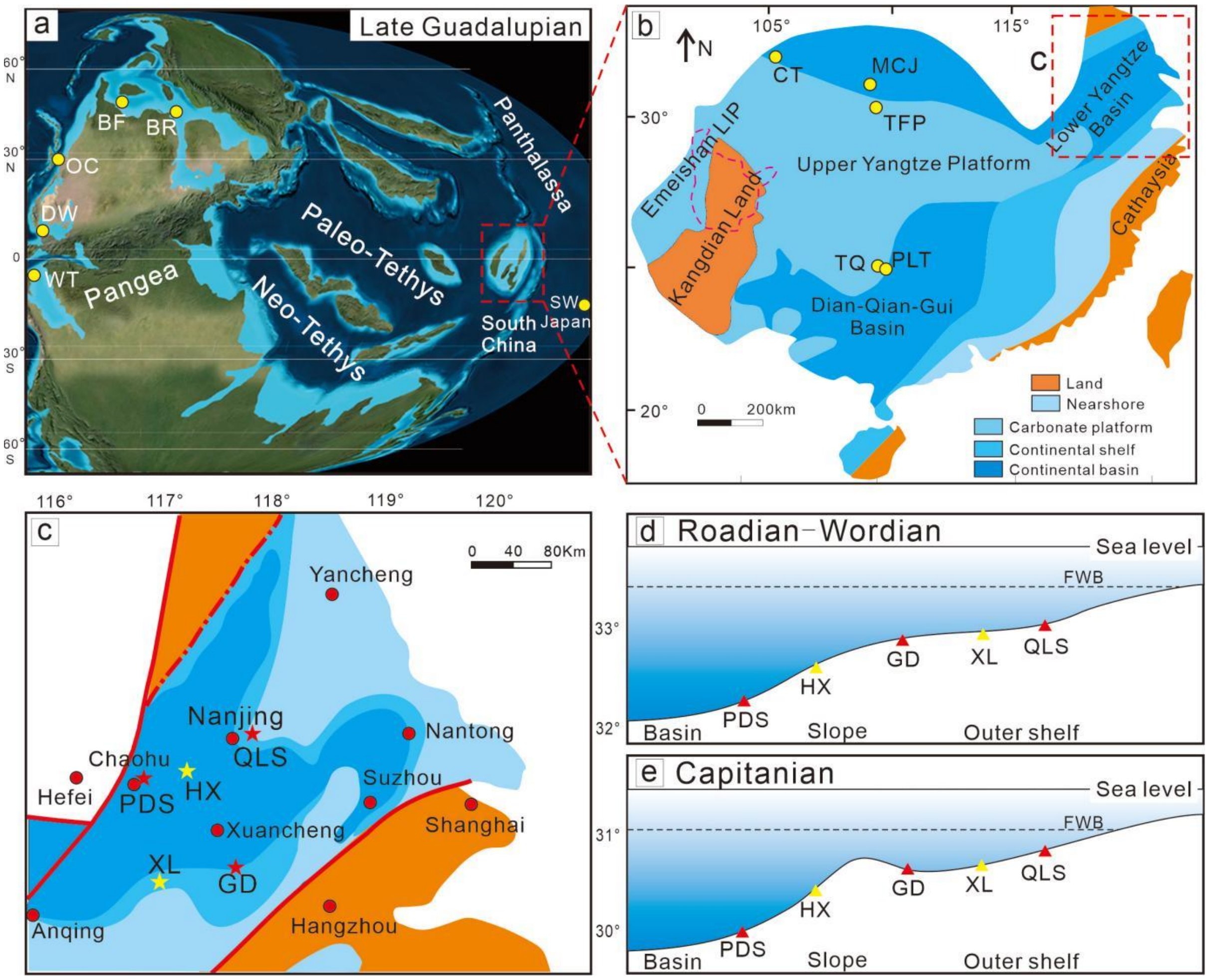
a
Late Guadalupian
60° N
30° N
0
30° S
60° S
BF
BR
OC
DW
WT
Pangea
Paleo-Tethys
Neo-Tethys
Panthalassa
South China
SW Japan
b
105°
115°
30°
20°
N
CT
MCJ
TFP
C
Lower Yangtze Basin
Emeishan LIP
Kangdian Land
Upper Yangtze Platform
Cathaysia
TQ
PLT
Dian-Qian-Gui Basin
0 200km
Land
Nearshore
Carbonate platform
Continental shelf
Continental basin
116°
117°
118°
119°
120°
c
0 40 80Km
Yancheng
Nanjing
QLS
Nantong
Chaohu
Hefei
PDS
HX
Suzhou
Xuancheng
Shanghai
XL
GD
Anqing
Hangzhou
d Roadian-Wordian
Sea level
FWB
33°
32°
PDS
HX
GD
XL
QLS
Basin
Slope
Outer shelf
e Capitanian
Sea level
FWB
31°
30°
PDS
HX
GD
XL
QLS
Basin
Slope
Outer shelf

Fig. 2.

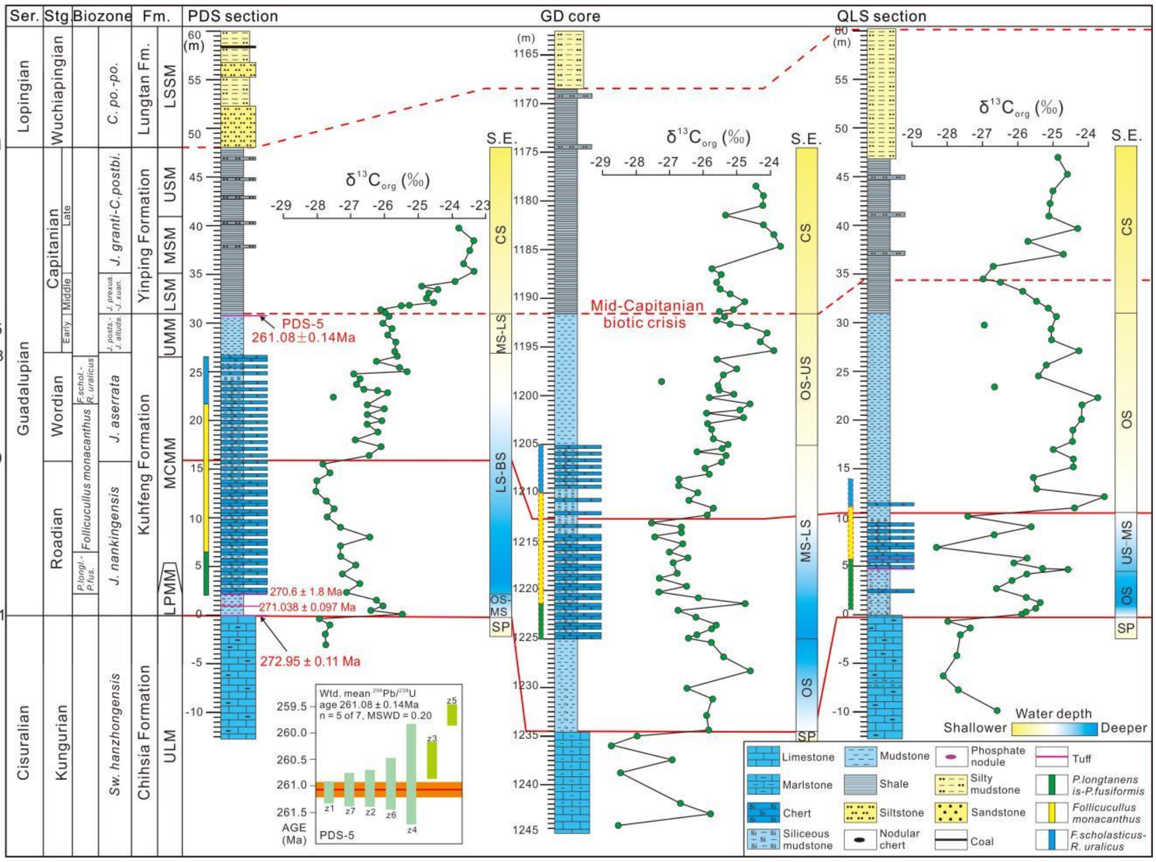
Age (Ma)
Ser.
Stg.
Biozone
Fm.
PDS section
GD core
QLS section
Lopingian
Wuchiapingian
Guadalupian
Capitanian
Wordian
Roadian
Cisuralian
Kungurian
Late
Middle
Early
C. po.-po.
J. granti-C.postbi.
J. aserrata
J. nankingensis
Sw. hanzhongensis
Follicucullus monacanthus
Lungtan Fm.
Yinping Formation
Kuhfeng Formation
Chihsia Formation
LSSM
USM
MSM
LSM
UMM
MCMM
LPMM
ULM
259.1
262.5
264.28
266.9
273.01
S.E.
CS
MS-LS
LS-BS
OS-MS
SP
OS-US
OS
US-MS
δ13Corg (‰)
PDS-5
261.08±0.14Ma
270.6 ± 1.8 Ma
271.038 ± 0.097 Ma
272.95 ± 0.11 Ma
Mid-Capitanian biotic crisis
Wtd. mean 206Pb/238U
age 261.08 ± 0.14Ma
n = 5 of 7, MSWD = 0.20
AGE (Ma)
Shallower
Water depth
Deeper
Limestone
Marlstone
Chert
Siliceous mudstone
Mudstone
Shale
Siltstone
Nodular chert
Phosphate nodule
Silty mudstone
Sandstone
Coal
Tuff
P.longtanensis-P.fusiformis
Follicucullus monacanthus
F.scholasticus-R. uralicus

Fig. 3.

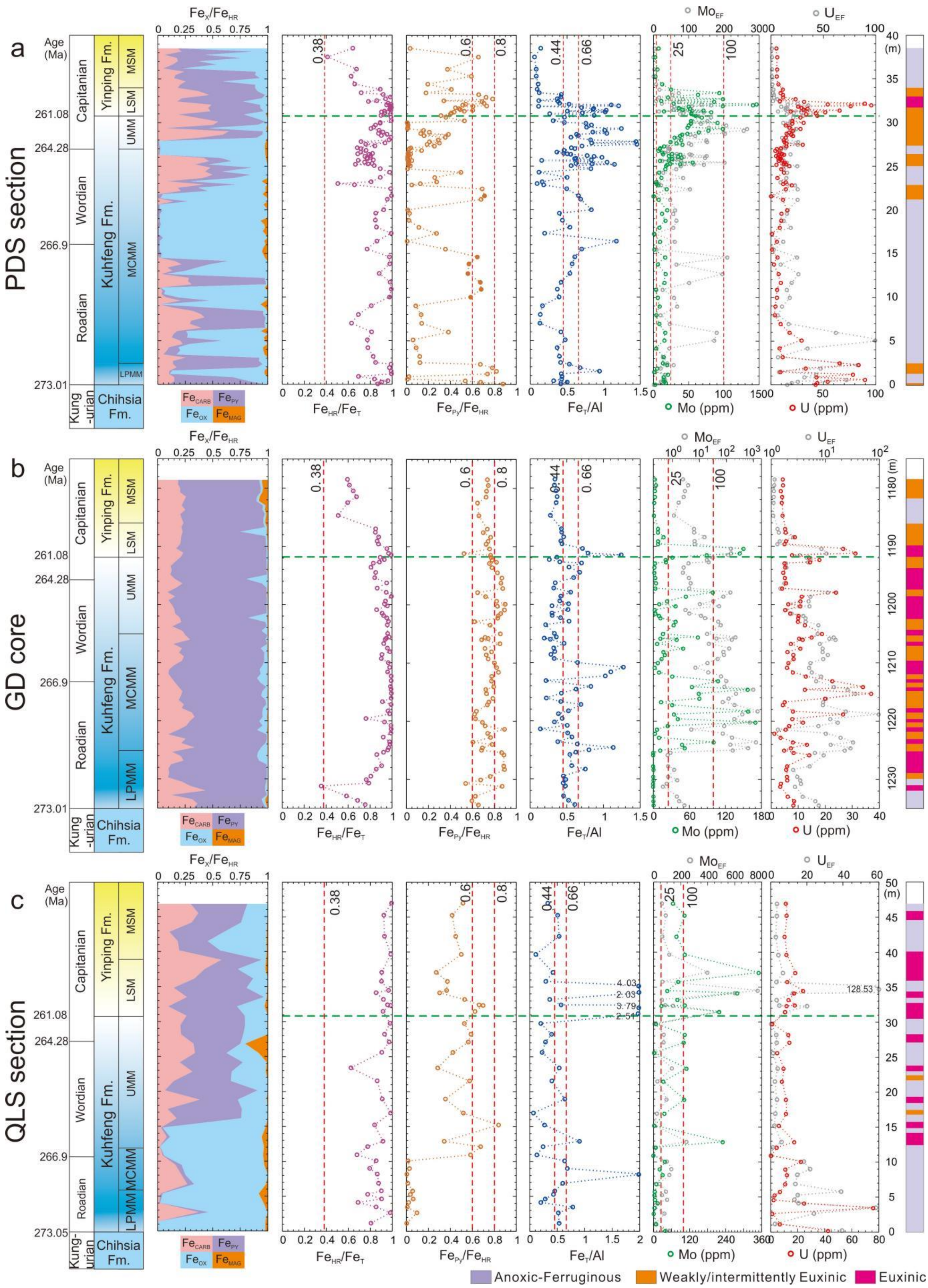
a
b
c
PDS section
GD core
QLS section
Age (Ma)
Capitanian
Wordian
Roadian
Kung-urian
Yinping Fm.
Kuhfeng Fm.
Chihsia Fm.
MSM
LSM
UMM
MCMM
LPMM
261.08
264.28
266.9
273.01
273.05
Fe_X/Fe_{HR}
Fe_{CARB}
Fe_{PY}
Fe_{OX}
Fe_{MAG}
Fe_{HR}/Fe_T
Fe_{Py}/Fe_{HR}
Fe_T/Al
Mo_{EF}
Mo (ppm)
U_{EF}
U (ppm)
(m)
0.38
0.6
0.8
0.44
0.66
25
100
Anoxic-Ferruginous
Weakly/intermittently Euxinic
Euxinic

Fig. 4.

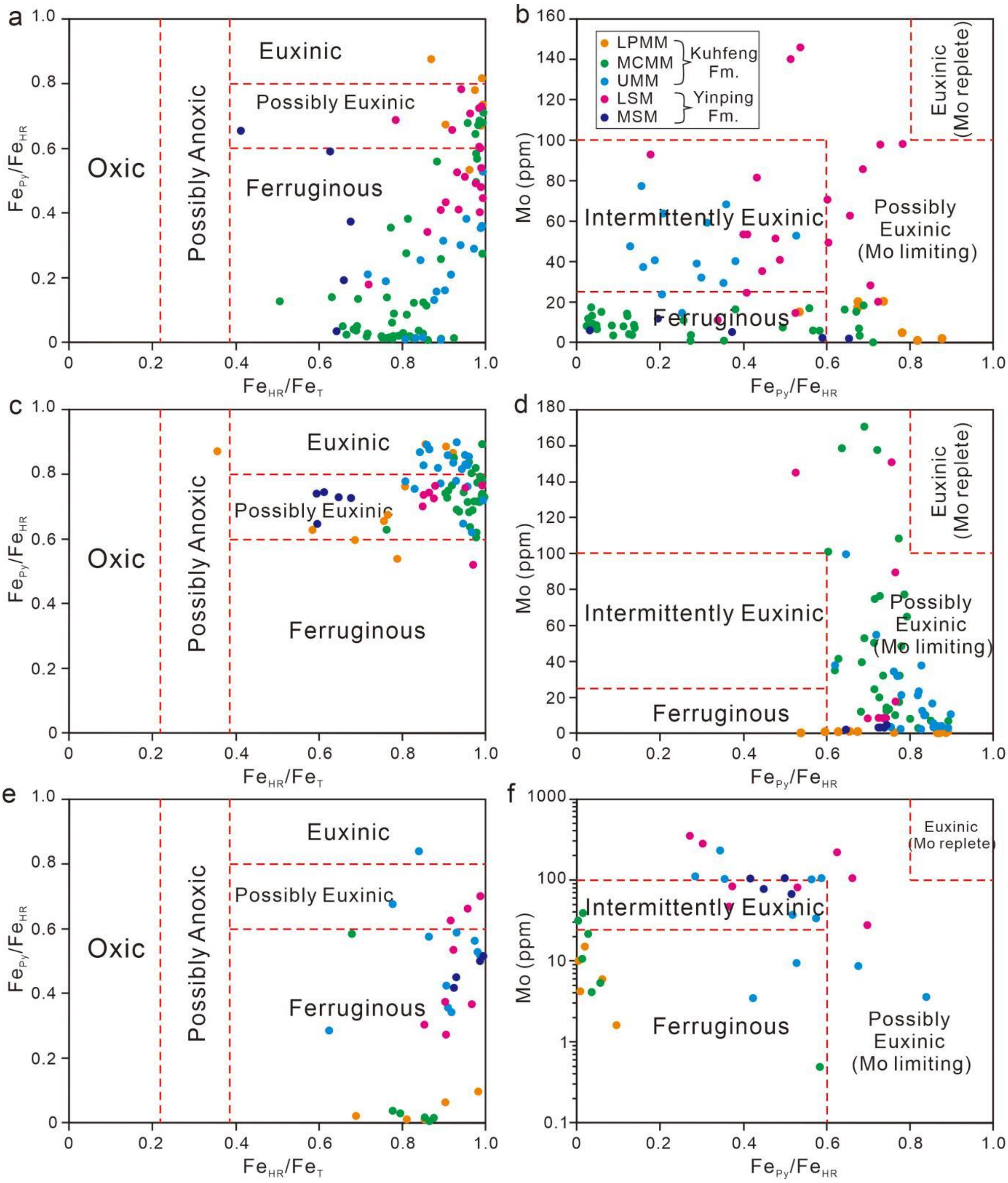
a
Euxinic
Possibly Euxinic
Oxic
Possibly Anoxic
Ferruginous
Fe_{Py}/Fe_{HR}
Fe_{HR}/Fe_T
b
LPMM
MCMM
UMM
Kuhfeng Fm.
LSM
MSM
Yinping Fm.
Euxinic (Mo replete)
Intermittently Euxinic
Possibly Euxinic (Mo limiting)
Ferruginous
Mo (ppm)
Fe_{Py}/Fe_{HR}
c
Euxinic
Possibly Euxinic
Oxic
Possibly Anoxic
Ferruginous
Fe_{Py}/Fe_{HR}
Fe_{HR}/Fe_T
d
Euxinic (Mo replete)
Intermittently Euxinic
Possibly Euxinic (Mo limiting)
Ferruginous
Mo (ppm)
Fe_{Py}/Fe_{HR}
e
Euxinic
Possibly Euxinic
Oxic
Possibly Anoxic
Ferruginous
Fe_{Py}/Fe_{HR}
Fe_{HR}/Fe_T
f
Euxinic (Mo replete)
Intermittently Euxinic
Ferruginous
Possibly Euxinic (Mo limiting)
Mo (ppm)
Fe_{Py}/Fe_{HR}

853 **Fig. 5.**

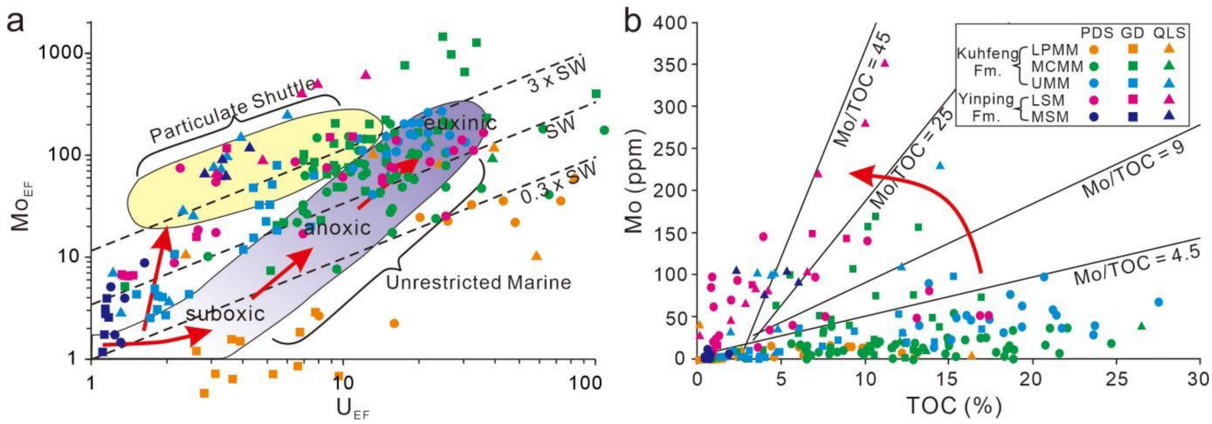

854

855

Fig. 6.

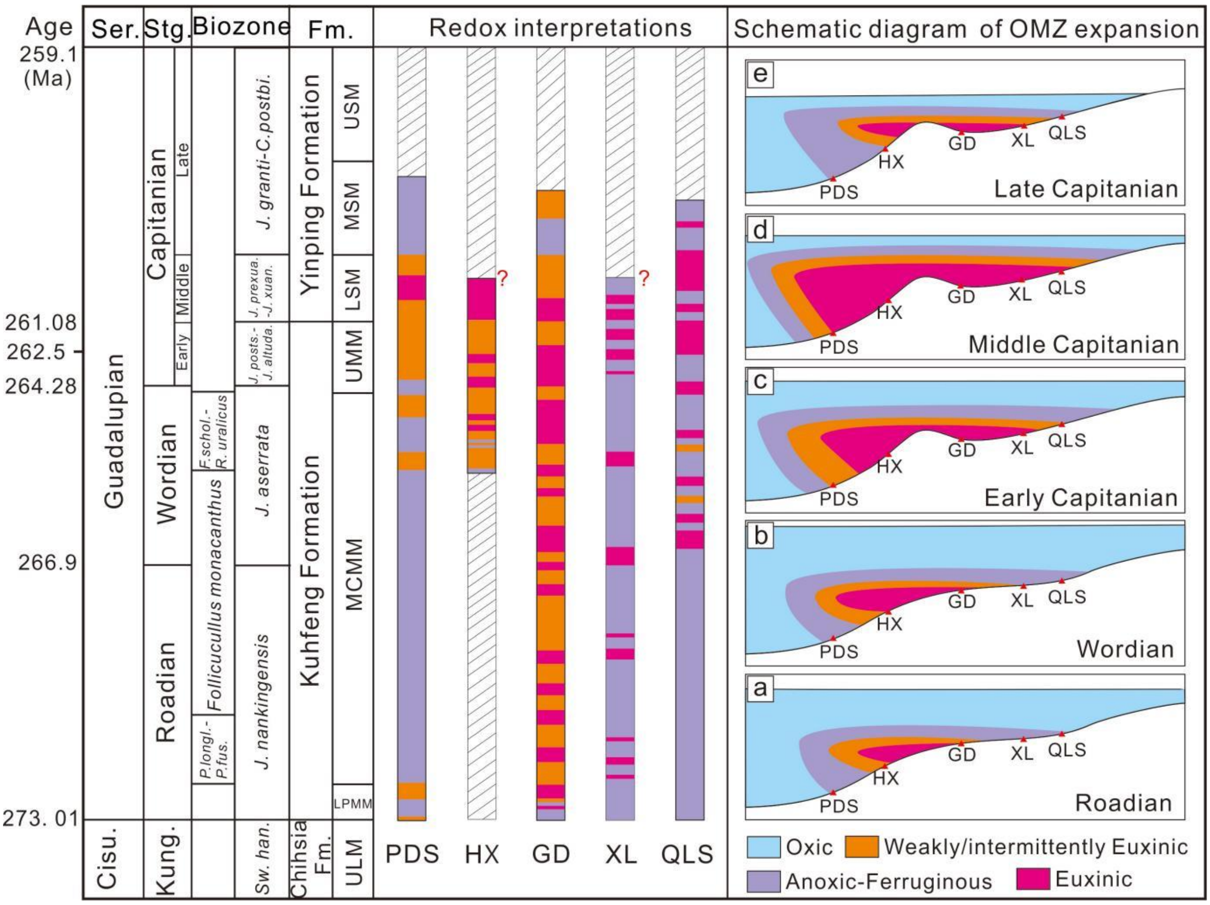
Age
259.1 (Ma)
261.08
262.5
264.28
266.9
273. 01
Ser.
Stg.
Biozone
Fm.
Redox interpretations
Schematic diagram of OMZ expansion
Guadalupian
Cisu.
Capitanian
Late
Middle
Early
Wordian
Roadian
Kung.
Follicucullus monacanthus
F.schol.-R. uralicus
P.longl.-P.fus.
J. granti-C.postbi.
J. prexua.-J. xuan.
J. posts.-J. altuda.
J. aserrata
J. nankingensis
Sw. han.
Yinping Formation
Kuhfeng Formation
Chihsia Fm.
USM
MSM
LSM
UMM
MCMM
LPMM
ULM
PDS
HX
GD
XL
QLS
e
Late Capitanian
d
Middle Capitanian
c
Early Capitanian
b
Wordian
a
Roadian
Oxic
Weakly/intermittently Euxinic
Anoxic-Ferruginous
Euxinic

859 **Fig. 7.**

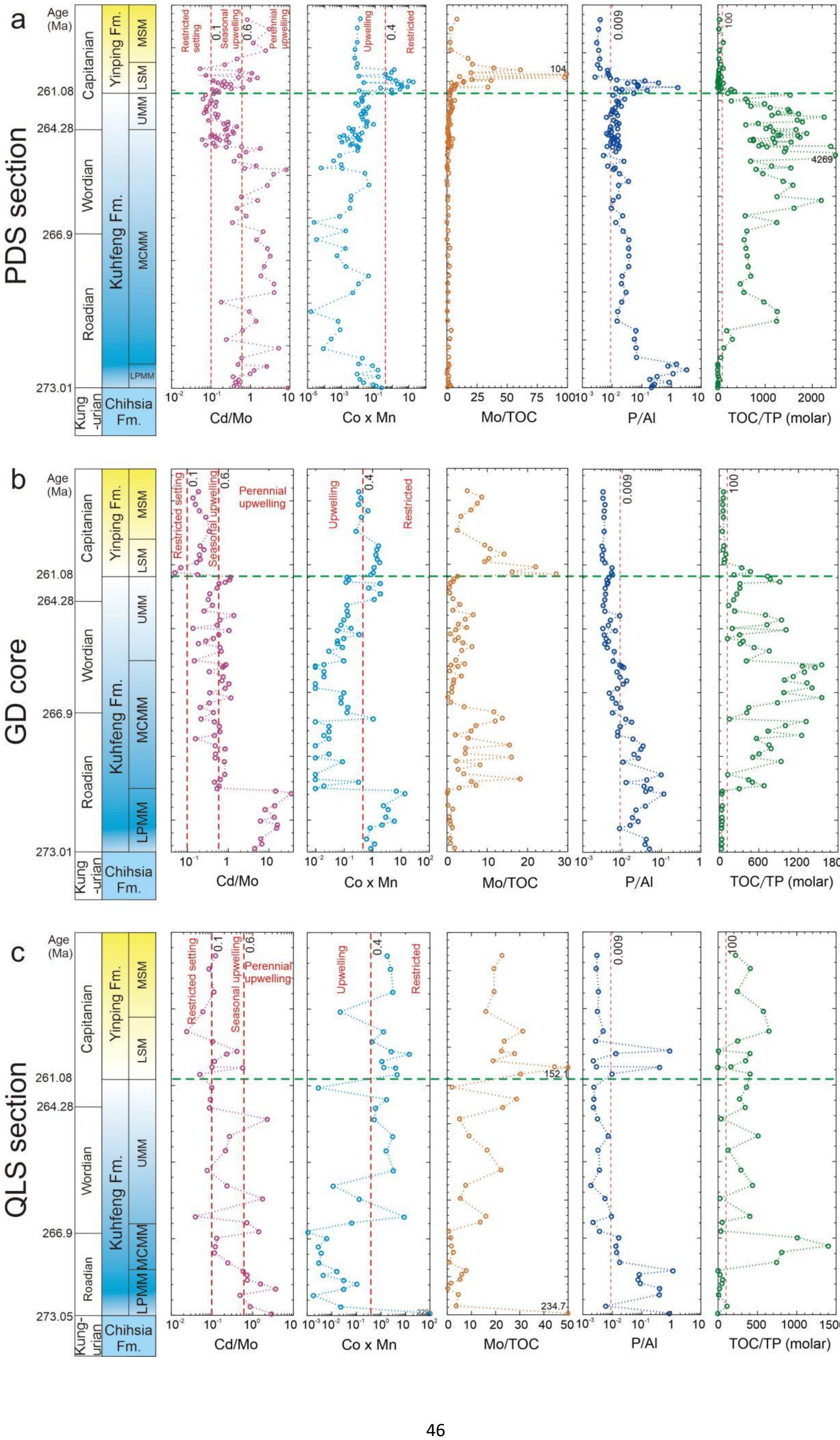
a
PDS section
GD core
QLS section
b
c
Age (Ma)
Capitanian
Wordian
Roadian
Kungurian
Yinping Fm.
Kuhfeng Fm.
Chihsia Fm.
MSM
LSM
UMM
MCMM
LPMM
261.08
264.28
266.9
273.01
273.05
Restricted setting
Seasonal upwelling
Perennial upwelling
Upwelling
Restricted
Cd/Mo
Co x Mn
Mo/TOC
P/Al
TOC/TP (molar)
0.009
100
104
4269
152.1
234.7
(m)

860

Fig. 8.

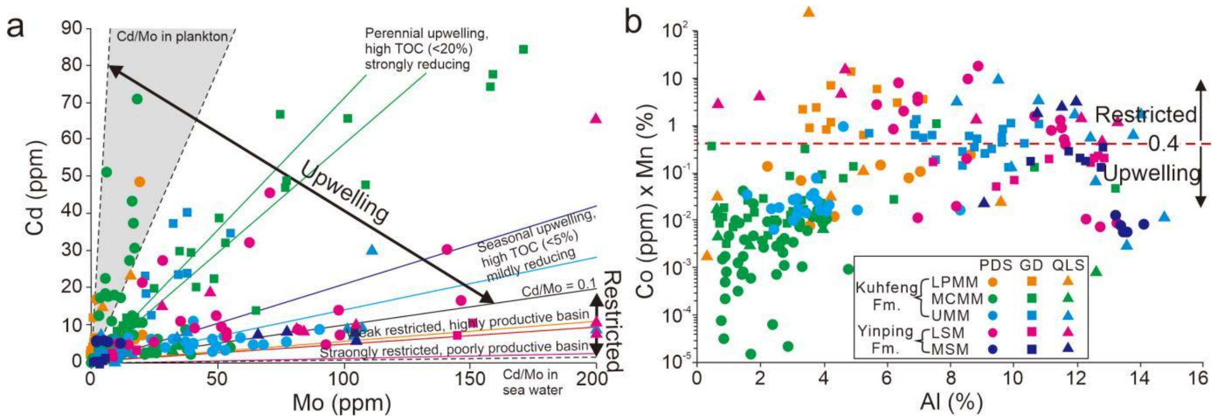
a
Cd/Mo in plankton
Perennial upwelling, high TOC (<20%) strongly reducing
Upwelling
Seasonal upwelling, high TOC (<5%) mildly reducing
Cd/Mo = 0.1
Weak restricted, highly productive basin
Straongly restricted, poorly productive basin
Cd/Mo in sea water
Restricted
Cd (ppm)
Mo (ppm)
b
Restricted
0.4
Upwelling
Co (ppm) x Mn (%)
Al (%)
PDS GD QLS
Kuhfeng Fm.
LPMM
MCMM
UMM
Yinping Fm.
LSM
MSM

Fig. 9.

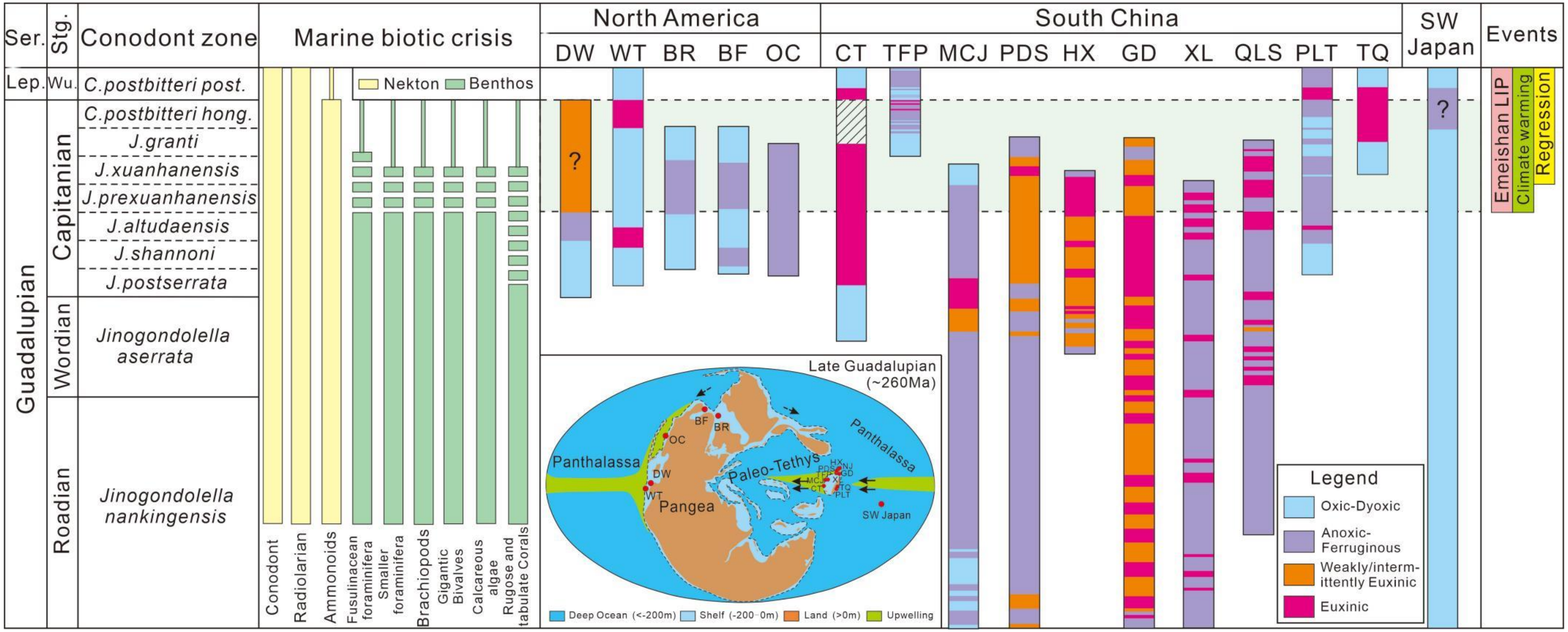
Ser.
Stg.
Conodont zone
Marine biotic crisis
North America
DW WT BR BF OC
South China
CT TFP MCJ PDS HX GD XL QLS PLT TQ
SW Japan
Events
Lep.
Wu.
C.postbitteri post.
Guadalupian
Capitanian
C.postbitteri hong.
J.granti
J.xuanhanensis
J.prexuanhanensis
J.altudaensis
J.shannoni
J.postserrata
Wordian
Jinogondolella aserrata
Roadian
Jinogondolella nankingensis
Nekton
Benthos
Conodont
Radiolarian
Ammonoids
Fusulinacean foraminifera
Smaller foraminifera
Brachiopods
Gigantic Bivalves
Calcareous algae
Rugose and tabulate Corals
?
Emeishan LIP
Climate warming
Regression
Late Guadalupian (~260Ma)
Panthalassa
Paleo-Tethys
Pangea
SW Japan
Deep Ocean (<-200m)
Shelf (-200~0m)
Land (>0m)
Upwelling
Legend
Oxic-Dyoxic
Anoxic-Ferruginous
Weakly/intermittently Euxinic
Euxinic